TKK Dissertations 235
Espoo 2010

ELECTROMAGNETIC AND MECHANICAL FINITE ELEMENT ANALYSIS OF END REGION OF LARGE-SIZED THREE-PHASE SQUIRREL-CAGE INDUCTION MACHINES

Doctoral Dissertation

Ranran Lin
林然然

Aalto University
School of Science and Technology
Faculty of Electronics, Communications and Automation
Department of Electrical Engineering

TKK Dissertations 235
Espoo 2010

ELECTROMAGNETIC AND MECHANICAL FINITE ELEMENT ANALYSIS OF END REGION OF LARGE-SIZED THREE-PHASE SQUIRREL-CAGE INDUCTION MACHINES

Doctoral Dissertation

Ranran Lin
林然然

Doctoral dissertation for the degree of Doctor of Science in Technology to be presented with due permission of the Faculty of Electronics, Communications and Automation for public examination and debate in Auditorium S4 at the Aalto University School of Science and Technology (Espoo, Finland) on the 17th of September 2010 at 12 noon.

Aalto University
School of Science and Technology
Faculty of Electronics, Communications and Automation
Department of Electrical Engineering

Aalto-yliopisto
Teknillinen korkeakoulu
Elektroniikan, tietoliikenteen ja automaation tiedekunta
Sähkötekniikan laitos

Distribution:
Aalto University
School of Science and Technology
Faculty of Electronics, Communications and Automation
Department of Electrical Engineering
P.O. Box 13000 (Otakaari 5)
FI - 00076 Aalto
FINLAND
URL: http://sahkotekniikka.tkk.fi/en/
Tel. +358-9-47001
Fax +358-9-470 22991
E-mail: ranran.lin@gmail.com

ISBN 978-952-60-3285-6
ISBN 978-952-60-3286-3 (PDF)
ISSN 1795-2239
ISSN 1795-4584 (PDF)
URL: http://lib.tkk.fi/Diss/2010/isbn9789526032863/

TKK-DISS-2792

Picaset Oy
Helsinki 2010

Aalto University

ABSTRACT OF DOCTORAL DISSERTATION	AALTO UNIVERSITY SCHOOL OF SCIENCE AND TECHNOLOGY P.O. BOX 11000, FI-00076 AALTO http://www.aalto.fi

Author Ranran Lin 林然然

Name of dissertation

Electromagnetic and Mechanical Finite Element Analysis of End Region of Large-Sized Three-Phase Squirrel-Cage Induction Machines

Manuscript submitted 31 March 2010	Manuscript revised 28 June 2010
Date of defence 17 September 2010	
☐ Monograph	☒ Article dissertation (summary + original articles)
Faculty	Faculty of Electronics, Communications and Automation
Department	Department of Electrical Engineering
Field of research	Electromechanics
Opponent	Antonios Kladas
Supervisor	Antero Arkkio
Instructor	

Abstract

This piece of research is related to the design of large-sized radial flux electric machines. It aims at studying the end-region magnetic field under the steady-state operation in order for an analysis of some important electromagnetic and mechanical phenomena that require careful thought during the design of the end region.

The research work is focused on the end region of two large-sized three-phase squirrel-cage induction machines. In addition to the end-region magnetic field, the stator end-winding leakage inductance, the eddy currents inside the end shield and the end frame, and the end-winding forces and vibrations are covered. The 3-D time-harmonic finite element analysis of the above aspects, carried out with a commercial software package, forms the main part of the research work. The corresponding measurement, as a complement to the finite element analysis, is mainly for validating the models and the numerical calculations.

A 3-D time-harmonic finite element analysis of the end-region magnetic field with suitable boundary conditions can give an accurate distribution of the magnetic field. The stator end-winding leakage only affects the core ends; hence, the end-winding leakage inductance can be calculated from the corresponding magnetic energy separated from the total magnetic energy. The eddy currents inside the end shield and the end frame do not affect the end-region magnetic field seriously, and it is feasible to consider them as surface currents and to model them with the standard impedance boundary condition. The end-winding forces cause vibrations and deformation, but the amplitude of vibration and the degree of deformation are small because of the end-winding bracing system. With the bracing system, the natural frequency of the most excitable mode of the end winding and its bracing system is also greatly raised, so resonances may be avoided.

Under the steady-state operation of large-sized induction machines, the end-region magnetic field does not bring about severely disadvantageous electromagnetic and mechanical phenomena in the end region. However, from the viewpoint of optimisation, the end frame can be shifted farther from the end winding for eliminating potential hot spots. In addition, fewer bracing parts can be fixed to the knuckle portion and the lower part of the involute portion of the end connections for improving the cooling of the end region.

Keywords eddy currents, end winding, induction machine, leakage flux, leakage inductance, vibration

ISBN (printed) 978-952-60-3285-6	ISSN (printed) 1795-2239
ISBN (PDF) 978-952-60-3286-3	ISSN (PDF) 1795-4584
Language English	Number of pages 74 + 46
Publisher Department of Electrical Engineering, Aalto University	
Print distribution Department of Electrical Engineering, Aalto University	
☒ The dissertation can be read at http://lib.tkk.fi/Diss/2010/isbn9789526032863/	

Preface

This piece of research began in May 2006. Before the end of 2009, the research work had been carried out at the Department of Electrical Engineering, Helsinki University of Technology. At the beginning of 2010, Helsinki University of Technology, Helsinki School of Economics, and University of Art and Design Helsinki were merged into Aalto University; hence, since then, the research work has been conducted at the Department of Electrical Engineering, Aalto University.

First of all, I am indebted to my supervisor, Prof Antero Arkkio, who guided me throughout the whole of my research work. Prof Arkkio proposed many invaluable suggestions and corrected many of my mistakes during the research work. I have learnt quite a lot from the discussions with him.

I am most grateful to Prof Asko Niemenmaa, the head of the department, for his support and encouragement. I would like to express my gratitude to Emeritus Prof Tapani Jokinen and Dr Anouar Belahcen for the discussions with them, and to Dr Jarmo Perho, the former laboratory manager, for the selection of my research topic. Prof Jorma Kyyrä, a vice rector of Aalto University, is specially thanked for his warm-hearted help. Mr Ari Haavisto, an operations engineer of the department, deserves my gratitude for helping me with a lot of daily work as well as some measurement. Mr Ilkka Hanhivaara, the laboratory technician of the department, is thanked for helping me with the preparation of some measurement. Ms Marika Schröder, a former secretary of the department, and Ms Anja Meuronen and Ms Terhi Arvela, secretaries of the department, are also thanked for their nice help. In addition, my thanks go to all of my colleagues, with whom I had so many useful discussions and so much fun.

Dr Antti Laiho, who is working in VTT Technical Research Centre of Finland, deserves my grateful thanks for his help in vibration measurement. Dr Janne Roivainen and Dr Timo Holopainen, who are working in ABB Corporation in Helsinki, Finland, are also thanked for their invaluable comments on one of my papers.

I thank my Chinese colleagues working in the department, Dr Xiaozhi Gao, Dr Xiaolei Wang, and Mr Zengcai Qu, as well as some former Chinese visiting scholars in the department, Dr Wei Chen from Tianjin University, and Mr Gang Liu from Jixi University.

The technical support of COMSOL Group is appreciated, and in particular, I am grateful to Mr Pasi Marttila, Mr Sakari Lukkarinen, Dr Erik Danielsson, and Ms Anna Dzougoutov.

I am much obliged to Prof Stefan Kulig from TU Dortmund University in Germany and Prof Erich Schmidt from Vienna University of Technology in Austria for their

invaluable comments on the manuscript of this doctoral thesis.

Graduate School in Electrical Energy Engineering in Finland is thanked for my course study. Moreover, Finnish Foundation for Technology Promotion (Tekniikan edistämissäätiö) and Research Foundation of Helsinki University of Technology (Teknillisen korkeakoulun tukisäätiö) are thanked for the financial support. Special thanks go to China Scholarship Council for the award given to me.

Last but not least, I would like to express my sincere gratitude to my grandmother, Ms Jingfang Li, my parents, Mr Dezhong Lin and Ms Aixiao Li, and my wife, Ms Xuemei Qiu, for their support, care, and love. They play an important role in my life, study, and work.

Espoo, Finland, July 2010

Ranran Lin

Contents

Preface **5**

Contents **7**

List of Publications **9**

Author's contribution **11**

List of Abbreviations **13**

List of Symbols **15**

1 Introduction **19**
1.1 Background to Research 19
1.2 Aim of Research 21
1.3 Scope of Research 21
1.4 Scientific Contributions 23
1.5 Structure of Compendium 24

2 Review of Relevant Literature **25**
2.1 End-Region Magnetic Field 25
2.2 Eddy Currents in End Region and Core Ends 28
2.3 Stator End-Winding Inductance 29
2.4 End-Winding Forces and Vibrations 31
2.5 Summary 34

3 Basic Introduction to Finite Element Analysis **36**
3.1 Finite Element Analysis of End-Region Magnetic Field 36
3.2 Finite Element Analysis of End-Winding Vibrations 38

4 Electromagnetic Analysis of End Region **41**
4.1 End-Region Magnetic Field 41
4.2 Stator End-Winding Inductance 45
4.3 Eddy Currents inside End Shield and End Frame 48

5 Mechanical Analysis of End Region **53**
5.1 End-Winding Magnetic Forces 53
5.2 End-Winding Mechanical Vibrations 55

6 Conclusions and Discussions **60**
6.1 Main Results of Research 60
6.2 Scientific Significance of Research 61
6.3 Accuracy of Research Methods 62

Appendix A Main Parameters of Electric Machines

Errata

List of Publications

This doctoral thesis consists of two parts: a compendium, and a collection of relevant publications. The publications are listed below and are referred to in the text by their Roman numerals.

I Lin, R., Haavisto, A., and Arkkio, A. (2009). Validation of a time-harmonic numerical model for solving magnetic field in end region of a radial-flux machine. *IEEE T Magn*, 45(12):5360–5367.

II Lin, R. and Arkkio, A. (2009). Calculation and analysis of stator end-winding leakage inductance of an induction machine. *IEEE T Magn*, 45(4):2009–2014.

III Lin, R., Haavisto, A., and Arkkio, A. (2010). Analysis of eddy-current loss in end shield and frame of a large induction machine. *IEEE T Magn*, 46(3):942–948.

IV Lin, R. and Arkkio, A. (2008). 3-D finite element analysis of magnetic forces on stator end-windings of an induction machine. *IEEE T Magn*, 44(11):4045–4048.

V Lin, R., Laiho, A. N., Haavisto, A., and Arkkio, A. (2010). End-winding vibrations caused by steady-state magnetic forces in an induction machine. *IEEE T Magn*, 46(7):2665–2674.

Author's contribution

The author of this doctoral thesis carried out most of the research work independently. He is the first-named author of the above publications, so he is responsible for most of the contents of the publications. The co-authors of the publications carried out the measurement related to the research work reported in the publications with the first-named author, gave the first-named author constructive ideas for the research work reported in the publications, and made invaluable comments on the contents of the publications.

The following is a summary of the first-named author's and the co-authors' contribution to each of the above publications, which has been recognised by all the co-authors.

- Publication I was fully written by the first-named author. Haavisto, A. and the first-named author performed the corresponding measurement of the electromagnetic field together. Arkkio, A. gave the first-named author constructive ideas for the research work reported in the publication and made invaluable comments on the contents of the publication.
- Publication II was fully written by the first-named author. Arkkio, A. gave the first-named author constructive ideas for the research work reported in the publication and made invaluable comments on the contents of the publication.
- Publication III was fully written by the first-named author. Haavisto, A. and the first-named author performed the corresponding measurement of the electromagnetic field together. Arkkio, A. gave the first-named author constructive ideas for the research work reported in the publication and made invaluable comments on the contents of the publication.
- Publication IV was fully written by the first-named author. Arkkio, A. gave the first-named author constructive ideas for the research work reported in the publication and made invaluable comments on the contents of the publication.
- Publication V was fully written by the first-named author. Laiho, A. N. and the first-named author performed the modal testing and the operating deflection shape measurement of the end-winding together. Laiho, A. N. also performed the data processing relating to the modal testing and the measurement. Haavisto, A. and the first-named author performed the corresponding measurement of the electromagnetic field together. Laiho, A. N. and Arkkio, A. both gave the first-named author constructive ideas for the research work reported in the publication and made invaluable comments on the contents of the publication.

List of Abbreviations

BVP	boundary value problem
CMP	correlated mode pair
DFT	discrete Fourier transform
DOF	degree of freedom
EMF	electromotive force
FDM	finite difference method
FEA	finite element analysis
FEM	finite element method
FRF	frequency response function
LTI	linear time-invariant
MAC	modal assurance criterion
ODS	operating deflection shape
PM	permanent-magnet
SIBC	standard impedance boundary condition
VPI	vacuum pressure impregnation
rms	root-mean-square

List of Symbols

$\boldsymbol{A}$	magnetic vector potential [Wb/m]
A_r, A_φ, A_z	r-, φ-, and z-component of $\boldsymbol{A}$ [Wb/m]
$\boldsymbol{B}$	magnetic induction [T]
$\boldsymbol{C}$	viscous damping matrix [N·s/m]
C_{jk}	entry of $\boldsymbol{C}$ [N·s/m]
$\boldsymbol{D}$	electric flux density [C/m^2]
D	Rayleigh's dissipation function [J/s]
$\boldsymbol{E}$	electric field strength [V/m]
$\mathscr{E}_{\mathrm{act}}$	induced EMF of search coil in active region [V]
$\mathscr{E}_{\mathrm{end}}$	induced EMF of search coil in end region [V]
E_{k}	kinetic energy [J]
E_{s}	strain energy [J]
E_{p}	potential energy [J]
$\boldsymbol{F}$	column vector of external force [N]
$\boldsymbol{F}_{\mathrm{ew}}$	end-winding force [N]
$\boldsymbol{F}_{\mathrm{exc}}$	column vector of excitation force [N]
$\boldsymbol{F}_i$	force on segment i [N]
$F_{i,r}, F_{i,\varphi}, F_{i,z}$	r-, φ-, and z-component of $\boldsymbol{F}_i$ [N]
$F_{i,r,\sim}, F_{i,\varphi,\sim}, F_{i,z,\sim}$	double-frequency component of $F_{i,r}$, $F_{i,\varphi}$, and $F_{i,z}$ [N]
F_j	external force associated with q_j [N]
$\boldsymbol{H}$	magnetic field strength [A/m]
$\boldsymbol{J}$	conduction current density [A/m^2]
$\boldsymbol{J}_{\mathrm{s}}$	source current density [A/m^2]
$\boldsymbol{J}_{\mathrm{sur}}$	surface current density [A/m]
$\boldsymbol{K}$	stiffness matrix [N/m]
K_{jk}	entry of $\boldsymbol{K}$ [N/m]
$L^{\mathrm{str}}_{\sigma,\mathrm{end}}$	stator end-winding inductance per phase [H]
$\boldsymbol{M}$	mass matrix [kg]
M_{jk}	entry of $\boldsymbol{M}$ [kg]
N	number of generalised coordinates
P_{Ft}	eddy-current loss [W]
$P^{\varphi}_{\mathrm{Ft}}$	eddy-current loss per unit circumferential length [W/m]
Q_j	generalised force associated with q_j [N]
R^{str}	resistance of stator phase winding [Ω]
S	surface area [m^2]
$\boldsymbol{T}$	electric vector potential [A/m]
T_z	z-component of $\boldsymbol{T}$ [A/m]
T_1	period of fundamental frequency [s]
V	electric scalar potential [V]
V	volume [m^3]
V_i	volume of segment i [m^3]
$W^{\mathrm{reg}}_{\mathrm{m,act}}$	magnetic energy in active region [J]

$W_{\mathrm{m,act}}^{\mathrm{src}}$	magnetic energy associated with coil sides [J]
$W_{\mathrm{m,end}}^{\mathrm{reg}}$	magnetic energy in end region [J]
$W_{\mathrm{m,end}}^{\mathrm{src}}$	magnetic energy associated with end connections [J]
$W_{\mathrm{m,tot}}$	total magnetic energy [J]
Z_{s}	surface impedance [Ω]
c_{stl}	specific heat capacity of steel [J/(kg·K)]
$\boldsymbol{f}_i$	force density of segment i [N/m^3]
$f_{i,r}, f_{i,\varphi}, f_{i,z}$	r-, φ-, and z-component of $\boldsymbol{f}_i$ [N/m^3]
i	index
i^{str}	current of stator phase winding [A]
j	index
j	imaginary unit
k	index
k_{Fe}	stacking factor of core
$l_{\mathrm{Fe}}^{\mathrm{str}}$	stator core length [m]
m	number of phases
$\boldsymbol{n}$	normal unit vector
p	number of pole pairs
p_{d}	dissipated power density [W/m^3]
$\boldsymbol{q}$	column vector of generalised coordinate
q_j, q_k	generalised coordinates j and k
r	radial coordinate
s	slip
t	time [s]
$\boldsymbol{u}$	column vector of displacement [m]
u^{str}	voltage of stator phase winding [V]
z	axial coordinate
Γ	surface of integration
Δt	incremental time [s]
$\Delta\vartheta$	incremental temperature [K]
Ω	domain of integration
$\vartheta_{i,r0}, \vartheta_{i,\varphi 0}, \vartheta_{i,z0}$	phase angle of $F_{i,r,\sim}$, $F_{i,\varphi,\sim}$, and $F_{i,z,\sim}$ [rad]
μ	permeability [H/m]
$\boldsymbol{\nu}$	tensor reluctivity [m/H]
$\nu_{\mathrm{Fe},z}$	axial reluctivity of core [m/H]
ν_{lam}	reluctivity of lamination [m/H]
ν_0	reluctivity of vacuum [m/H]
ϱ_{stl}	mass density of steel [kg/m^3]
$\boldsymbol{\sigma}$	tensor conductivity [S/m]
σ	conductivity [S/m]
ϕ	magnetic scalar potential [A]
φ	circumferential coordinate
$\boldsymbol{\psi}_{\mathrm{calc}}$	column vector of calculated mode shape
$\boldsymbol{\psi}_{\mathrm{exp}}$	column vector of experimental mode shape

$\psi_{\mathrm{act}}^{\mathrm{str}}$	flux linkage of stator phase winding in active region [Wb]
ω	angular frequency [rad/s]
ω_{s}	angular frequency of stator field [rad/s]

1 Introduction

This chapter forms an introduction to this compendium. The background to this piece of research is explained at the beginning, followed by the aim and the scope. The scientific contributions are briefly summarised at the end of this chapter.

1.1 Background to Research

In conventional ac rotating electric machines, such as synchronous machines and induction machines, the stator core and the rotor core are usually stacked with laminations made from non-oriented electrical steel sheets. The magnetic flux passing through the air gap is mainly in the radial direction, so these kinds of electric machines are referred to as radial flux electric machines. Figure 1.1 shows a diagram of a large-sized radial flux electric machine.

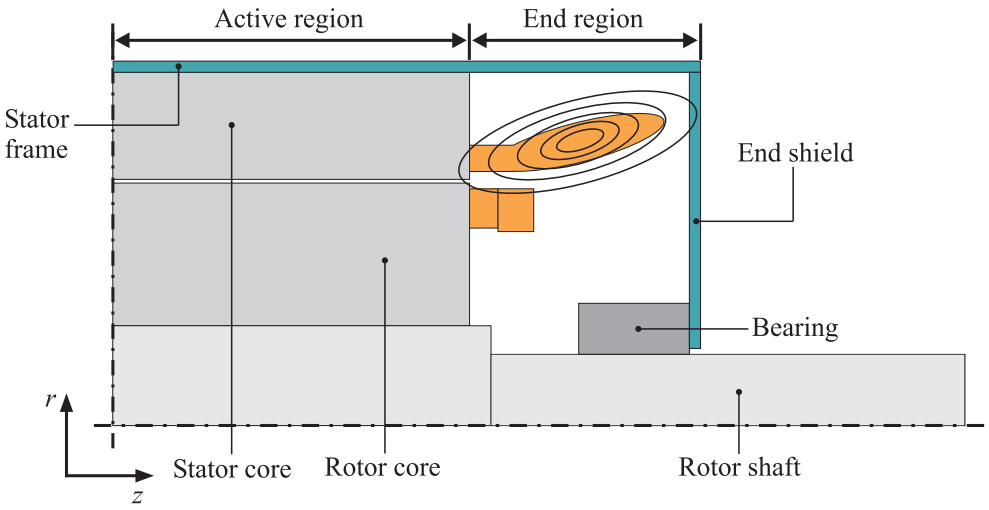

Figure 1.1: A diagram of half of the drive end of a large-sized radial flux electric machine (squirrel-cage induction machine).

Under the steady-state operation of radial flux electric machines, about 95% of the total magnetic flux is in the active region, and only around 5% in the end region. Therefore, their operating characteristics can be predicted relatively well even if the end-region magnetic field is totally omitted. However, under the transient operation, e.g. the starting of 3-phase induction motors, the extremely large starting current causes deep saturation of the laminated cores, which greatly increases the proportion of the end-region magnetic flux to the total magnetic flux. Under the circumstances,

the end-region magnetic field becomes relatively important for predicting the operating characteristics of these electric machines. In addition, in some large-sized radial flux electric machines, e.g. turbogenerators installed at power stations, even under the steady-state operation, the end-region magnetic field may cause some disadvantageous electromagnetic and mechanical phenomena, which might have a major effect on their operating characteristics. As a result, more attention must be paid to the end region of these large-sized electric machines.

When large-sized synchronous machines or induction machines run under a load, the end-region magnetic field comprises mainly four components. First, the most important one is the stator end-winding leakage, which is caused by the current flowing in the end connections[1] of the stator coils, as shown in Figure 1.1, since the end connections stretch deep into the end region. Second, the current flowing in the end portion of the field winding of wound field synchronous machines, and the current flowing in the rotor end winding of wound rotor induction machines or in the rotor end cage[2] of squirrel-cage induction machines cause leakage flux in the end region of these electric machines. Third, the end-region magnetic field induces eddy currents in the surrounding metal parts as well as in the core ends; conversely, those eddy currents may affect the end-region magnetic field. Finally, the air-gap fringing flux, as a part of the air-gap magnetic flux, is also distributed in the end region.

In general, the aforementioned eddy currents can give rise to resistive loss, and the loss can generate heat and might cause hot spots in some of the surrounding parts. The time-varying end-region magnetic field can cause magnetic forces on the end connections of the stator coils, which may excite mechanical vibrations that give rise to looseness of the end-winding bracing system, damage to the enamel on the surface of the end connections, and looseness of the stator coils especially in stators having a non-global vacuum pressure impregnation (VPI) process (Stone et al., 2009); conversely, the vibrations might slightly affect the end-region magnetic field. Moreover, the above heat and forces can cause stresses and strains in the end connections as well as in the parts surrounding them. Therefore, some of these phenomena can affect one another, and their main interactions are shown in Figure 1.2.

Since they become more serious under the transient operation, some of the above phenomena must be taken into consideration during the design of large-sized electric machines. On the other hand, the design of electric machines normally requires a calculation of the electromagnetic field, and the most important parameter associated with the end-region magnetic field is the stator end-winding leakage inductance. Its accurate value is particularly important because an accurate value can greatly raise the accuracy of both analytical models based on lumped parameter equiva-

[1] In this compendium, the definition of the term "end connections" is from reference (Gross, 2007), and the term "end connections" means the portion of a coil outside the slots.

[2] In this compendium, the term "rotor end cage" means the portion of a rotor cage outside the rotor slots, i.e. the end rings and the end bars.

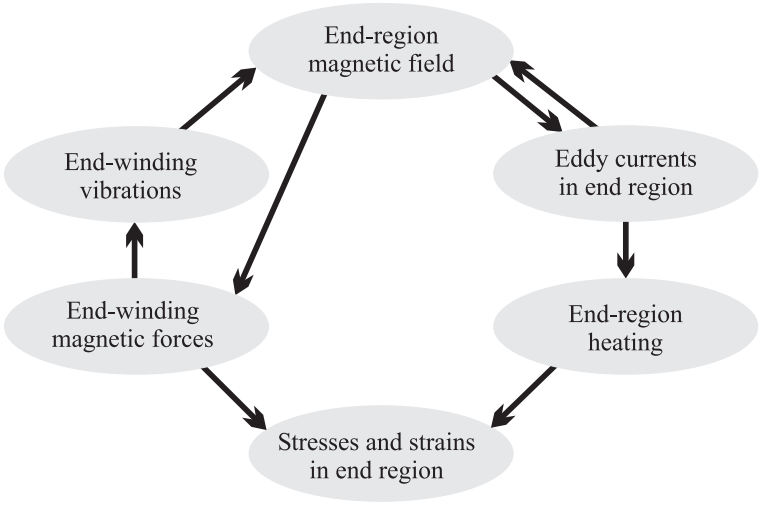

Figure 1.2: The interactions of the main phenomena in the end region of large-sized radial flux electric machines.

lent circuits and 2-D cross-sectional numerical models based on coupled field–circuit equations.

1.2 Aim of Research

This piece of research aims at calculating the end-region magnetic field in large-sized radial flux electric machines in order for an estimation of the stator end-winding leakage inductance and a detailed analysis of some important electromagnetic and mechanical phenomena arising in the end region, i.e. the eddy currents, the magnetic forces, the stresses, and the mechanical vibrations.

1.3 Scope of Research

Solving the 3-D end-region magnetic field in large-sized radial flux electric machines is at the core of this piece of research because the study of the above electromagnetic and mechanical phenomena is mainly dependent upon the solution to the magnetic field. With the aid of increasingly advanced computers, numerical methods have been widely applied to the calculation of the magnetic field in radial flux electric machines for several decades, but nowadays their application is still concentrated on the 2-D numerical analysis of the magnetic field in the active region. However, this piece of research is focused on the 3-D numerical analysis of the end-region magnetic field as well as the numerical analysis of the aforementioned eddy currents, magnetic

forces, stresses, and mechanical vibrations. The numerical analysis performed in this piece of research is based on the finite element method (FEM).

As the end-region magnetic field in large-sized radial flux electric machines is more important than that in small-sized ones, this piece of research places great emphasis on large-sized electric machines. Turbogenerators generally have a large size and a large capacity, but it is hard to study them in 3-D space with the FEM because of the large number of degrees of freedom (DOFs) in the course of solving their 3-D models. It is almost impossible to take any measurements of a turbogenerator in the laboratory for validating corresponding numerical calculations. As a result, this piece of research only covers large-sized 3-phase induction machines. In general, large-sized synchronous machines and induction machines both have similar form-wound multi-turn stator coils, as shown in Figure 1.3, and the main difference lies in the structure of the end portion of the rotor, which is normally not as important as the stator end winding.

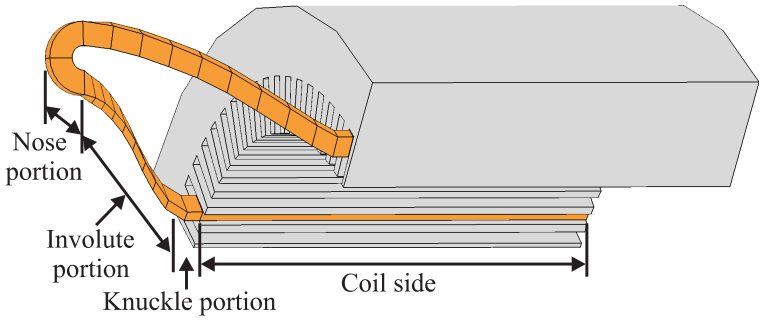

Figure 1.3: Half of a form-wound stator coil in the two-layer diamond winding of a radial flux electric machine.

For the sake of economy, electromechanical devices, e.g. rotating electric machines, are generally designed in such a way that the electrical steel sheets of the cores are into saturation during certain moments in each supply cycle (Williamson and Ralph, 1982). Although the saturation of the cores and the rotation of the rotor are usually taken into account in the 2-D finite element analysis (FEA) of the magnetic field in the active region, to consider them in the 3-D FEA of the end-region magnetic field is not easy, on account of the extremely long computation time. On the other hand, unlike the air-gap magnetic flux, the end-region magnetic flux forms closed loops mainly in the air and other non-magnetic substances, which means that the saturation is not a dominant factor. Consequently, in this piece of research, all 3-D calculations relating to the end-region magnetic field are based on time-harmonic FEAs, but a few 2-D calculations are based on time-discretised FEAs. By taking some necessary measurements as validations, the results obtained from the time-harmonic FEAs can be considered reliable.

1.4 Scientific Contributions

The following is a summary of the scientific contributions of this piece of research.

1. A linear model solved in a time-harmonic FEA is capable of estimating the 3-D end-region magnetic field in a large-sized induction machine accurately when the anisotropic effect of the laminated cores is considered and suitable boundary conditions are applied.

2. The proposed method of estimating the magnetic energy associated with the stator end-winding leakage in a large-sized induction machine is applicable since the stator end-winding leakage cannot penetrate the middle portion of the stator core. The stator end-winding inductance, which is used in the 2-D coupled field–circuit numerical models and analytical lumped parameter models, can be calculated from the corresponding magnetic energy.

3. It is feasible to model the eddy currents inside the end frame[3] and the end shield of a large-sized induction machine with the standard impedance boundary condition (SIBC). The method of estimating the eddy-current loss by measuring the temperature rise is also applicable. The eddy-current loss only accounts for a small portion of the total losses of an induction machine.

4. In a large-sized induction machine, the radial end-winding force density in the knuckle portion of the end connections is larger than that in the other portions. The end-winding forces on each of the end connections belonging to the same phase belt are somewhat different.

5. An undamped linear time-invariant (LTI) mechanical model is capable of obtaining the modal data of the end winding and its bracing system and of studying the end-winding vibrations of a large-sized induction machine when correct mechanical properties are given. The amplitude of vibration is small under the steady state, even in the nose portion, and the natural frequency of the most excitable mode is much higher than the excitation frequency.

The above five scientific contributions can be found in the corresponding publications in this thesis, as listed in Table 1.1 below.

Table 1.1: Scientific Contributions and Corresponding Publications.

Scientific contribution	1	2	3	4	5
Corresponding publication	I	II	III	IV, V	V

[3]In this compendium, the term "end frame" means the portion of a stator frame that lies in the end region.

1.5 Structure of Compendium

This compendium is organised according to the following structure.

- Chapter 1 forms an introduction to this compendium. The background to this piece of research, the aim, and the scope are explained. The corresponding scientific contributions are elaborated as well.
- Chapter 2 is intended as a review of the literature on the end-region magnetic field in large-sized radial flux electric machines as well as the corresponding eddy currents, magnetic forces, stresses, mechanical vibrations, etc.
- Chapter 3 outlines the FEA of the end-region magnetic field and the end-winding vibrations performed in this piece of research. The basic theory of electromagnetic fields and mechanical vibrations is briefly given as well.
- Chapter 4 forms a summary of the electromagnetic analysis of the end region in large-sized squirrel-cage induction machines, including an analysis of the end-region magnetic field, a calculation of the stator end-winding inductance, and an analysis of the eddy currents inside the end shield and the end frame.
- Chapter 5 forms a summary of the mechanical analysis of the end region in large-sized squirrel-cage induction machines, including an analysis of the end-winding forces and an analysis of the end-winding vibrations.
- Chapter 6 summarises the main results and discusses the scientific significance of this piece of research. Some issues relating to the accuracy of the research methods are also discussed.

2 Review of Relevant Literature

This chapter is intended as a review of the relevant literature on the end-region magnetic field in large-sized radial flux electric machines and related electromagnetic and mechanical phenomena. The review falls into roughly four categories. The first is focused on the end-region magnetic field; the second discusses the eddy currents and the corresponding eddy-current loss; the third is about the stator end-winding leakage inductance, and in the fourth category, the end-winding forces and the end-winding vibrations are covered. In general, none of the above four categories is totally independent, so there is some overlap among the categories.

2.1 End-Region Magnetic Field

Before numerical methods were put into use, analytical methods were the only means of calculating the end-region magnetic field in large-sized radial flux electric machines, and they are still in use nowadays. For instance, in references (Chow et al., 1982) and (Frei-Spreiter and Reichert, 1998), the end-region magnetic field was considered to be caused by two sources: the end connections of the stator coils and the magnetisation sources, e.g. the magnetic field in the rotor shaft (Frei-Spreiter and Reichert, 1998). The computation of both parts caused by the two sources was completed by analytical integral equations, but the eddy currents in the end region as well as in the stator core ends were not taken into consideration. In addition, in the analytical calculations, the end connections of the stator coils were usually replaced by a number of infinitely thin segments along their centrelines, e.g. in reference (Ban et al., 2005). In order for the inclusion of the effect of the stator core, the image method was used, and the images of the end connections were substituted for the stator core. For instance, Ban et al. (2005) and Schramm and Gerling (2005) illustrated a detailed procedure for the use of the image method.

Numerical methods like the FEM have been used in the study of the electromagnetic field in large-sized radial flux electric machines for several decades since they can deal with arbitrary shapes, arbitrary boundary conditions, and complicated or distributed sources (Salon, 1990). On account of the complex structure of the end region, a quasi-3-D method was used for simplifying the study, which means that the end-region magnetic field was considered to be a sinusoidal travelling wave propagating in the circumferential direction (Ho and Fu, 1998). Therefore, only the changes within the radial–axial plane required careful consideration (Ho and Fu, 1998). As a matter of fact, the spatial distribution of the end-region magnetic field is not simply sinusoidal in the circumferential direction by reason of the harmonics. However, to solve the end-region magnetic field in 3-D space requires plenty of computational resources and perhaps a great deal of computation time, in particular,

when time-discretised nonlinear FEAs are carried out.

Weiss and Stephens (1981) completed a 3-D magnetostatic analysis of the end-region magnetic field in a turbogenerator. The magnetic field was solved in such a way that it was decomposed into two components: one was rotational and caused by the current in the end connections, and the other was irrotational everywhere. The two components were solved from the magnetic vector potential and the magnetic scalar potential, respectively. The authors also took account of the effect of the slots and the teeth on the circumferential permeability of the core. Plantive et al. (1996) also conducted a magnetostatic analysis. They solved the end-region magnetic field in an 820-MVA generator by using the two-potential method[4].

An analysis of the end-region magnetic field in a 27-kVA synchronous generator was conducted by Richard et al. (1997), who used the two-potential method. The authors obtained a distribution of the magnetic induction above the nose portion of the end connections. They also found that the copper screen had a major effect on the magnitude and the distribution of the end-region magnetic field. In another analysis, in order to evaluate the leakage flux in the end region as well as in the stator core ends of a 1000-MW turbogenerator under different power factors, Fujita et al. (2000) proposed a relatively fast approach. They solved the magnetic field only under an open circuit and a short circuit by the two-potential method. By using phasor diagrams, they were able to evaluate the magnetic field under any power factor, both inductive and capacitive. In their calculation, the use of Biot-Savart's law kept the source currents excluded from the finite element mesh. In addition, as the involute portion of the end connections of form-wound coils is usually laid upon the surface of a fictitious cone with a certain conical angle (Holmberg, 1998), Li et al. (2005) solved the end-region magnetic field in a turbogenerator under different conical angles by using the two-potential method. In their study, the conical angle was varied from 30° to 31.5°, but the authors found that there was little influence on the distribution and the magnitude of the end-region magnetic field.

Sikora et al. (1982, 1986) solved the end-region magnetic field in an induction motor by using the FEM based on the $\boldsymbol{T}$–ϕ formulation, where $\boldsymbol{T}$ and ϕ denote the electric vector potential and the magnetic scalar potential, respectively. In their earlier study reported in reference (Sikora et al., 1982), the current density in the end connections was supposed to have an axial and a circumferential component. The authors calculated the magnetic field under two different boundary conditions applied to the stator core, the frame, etc., i.e. an infinitely permeable boundary condition ($\mu \to +\infty$) and an infinitely conductive one ($\sigma \to +\infty$), where μ and σ denote the permeability and the conductivity, respectively. Reference (Sikora et al., 1986) is a continuation of the earlier one. The authors improved their model by taking account of all three components of the current density in the end connections.

[4]In this compendium, the term "the two-potential method" means the method in which the total and the reduced magnetic scalar potential are used.

The nonlinear 3-D calculation of the end-region magnetic field has not been widely conducted yet on account of its extremely long computation time. However, Novender and Müller (1983) completed a nonlinear calculation of the end-region magnetic field in a 214-MVA turbogenerator by the finite difference method (FDM), in which single-valued B–H curves were used in the magnetic materials. The computation times of CPU for the no-load and the full-load calculation were around 61 h and 75 h, respectively.

Jack and Mecrow (1986, 1987) published two papers on the investigation into the end-region magnetic field in a 660-MW turbogenerator as well as its effect on the stator core. They used a quasi-3-D method and solved the magnetic field by using the FEM based on the $\boldsymbol{T}$–ϕ formulation. Nonlinear single-valued B–H curves were used in the ferromagnetic materials, and the eddy currents inside the stator core ends were considered. The authors mainly analysed the radial variations of the axial magnetic induction, i.e. from the tooth tip to the core back, in different positions of the stator core ends.

In large-sized radial flux electric machines equipped with form-wound multi-turn stator coils, the distribution of the current density over the cross-section of the conductors is non-uniform, and there are some circulating currents flowing in the conductors. Tang et al. (1990) analysed the end-region magnetic field in a 300-MW turbogenerator as well as the circulating currents in the coils by the FEM based on the $\boldsymbol{A}$–V formulation, where $\boldsymbol{A}$ and V denote the magnetic vector potential and the electric scalar potential, respectively. The authors pointed out that it was the circumferential and the radial component of the end-region magnetic field that caused the circulating currents.

Wen et al. (1994) analysed the end-region magnetic field in a 35-MW turbogenerator under a 3-phase short circuit by using a quasi-3-D method based on the $\boldsymbol{A}$–V formulation. The authors found that the eddy currents inside the retaining ring were important and not negligible during the transient calculation of the end-region magnetic field. Yao et al. (2006) conducted an analysis of the end-region magnetic field in a 1056-MVA turbogenerator with the FEM, in which the reduced magnetic vector potential was used. The modelling of the complicated source currents was avoided in the finite element mesh, and the magnetic field caused by the source currents was calculated from Biot-Savart's law instead. The topic of the end-region magnetic field in large-sized turbogenerators was also studied by Liang et al. (2003, 2008) and Yao et al. (2008), and the $\boldsymbol{A}$–V formulation was used in all the above three studies. Among them, Liang et al. (2003) dealt mainly with the magnetic field in the rotor end region.

A comparison of different methods of calculating the end-region magnetic field was drawn by Lazarns et al. (2009). From the viewpoint of the structural optimisation of electric machines, the comparison indicated that a method based on 2-D FEAs in which an axiperiodic distribution of the currents was supposed possessed acceptable

accuracy and modest computational requirements, by comparison with analytical methods, the image method, and methods based on 3-D FEAs. Then the method was applied to the geometric optimisation of the magnetic shields of a permanent-magnet (PM) machine for reducing the end-winding forces.

2.2 Eddy Currents in End Region and Core Ends

The end-region magnetic field in large-sized radial flux electric machines can induce eddy currents in the surrounding metal parts. The eddy currents inside the laminations of the core ends are also partly related to the end-region magnetic field. In general, it is quite difficult or impossible to study those eddy currents with analytical methods because of their complicated distribution; hence, they are mainly analysed with numerical methods.

Jack and Mecrow (1987) and Mecrow et al. (1989) jointly analysed the eddy currents caused by the axial flux in the stator core ends of turbogenerators with the FEM based on the $\boldsymbol{T}$–ϕ formulation. In reference (Jack and Mecrow, 1987), a quasi-3-D method was used and the authors found that the eddy currents were mainly concentrated around the end of the Pistoye slots on account of the slits. They also estimated the corresponding loss density in various positions of the end packets. In reference (Mecrow et al., 1989), the authors completed a thorough study of the axial flux causing eddy currents in the stator core ends of turbogenerators. They evaluated the importance of different sources causing the axial flux. Various factors related to the end-region magnetic field were also discussed, such as the stepped core ends and the change in the rotor core length. In particular, how the effect of these factors impinged upon the axial flux and the corresponding loss was discussed.

Khan et al. (1990) published a paper dealing with the eddy-current loss and the temperature caused by the axial flux in the stator core ends of a 1000-MW turbogenerator. They used a quasi-3-D method but took the nonlinear magnetic circuit into account. The authors mainly analysed the distribution of the axial magnetic induction in the end packets in both the axial and the radial direction as well as the distribution of the loss density in the axial direction. It was found that the double-slit stator teeth could reduce more eddy currents than the single-slit stator teeth. Silva et al. (1995a) especially analysed the effect of the slitting of the stator teeth in a 300-MVA generator. The authors did not take account of the saturation of the core. The eddy currents induced by the axial flux in the core ends were modelled by the SIBC, which was applied to the surface of the stator core ends. With the single-slit teeth, a remarkable drop in the eddy-current loss was found, but a slight increase in the loss in the stator core back was observed. In another study performed by Silva et al. (1996), the authors analysed the same eddy-current loss again with the FEM based on the $\boldsymbol{T}$–ϕ formulation. In comparison with reference (Silva et al., 1995a), part of the stator core with radial cooling ducts was included,

and the laminated core was treated as a homogeneous, anisotropic solid core. They mainly illustrated the distribution of the eddy currents as well as the distribution of the loss in the core ends.

Schmidt et al. (2005) published a paper on the effect of the harmonics of the end-region magnetic field on the eddy currents in the stator clamping system of a 450-MVA hydroelectric generator. Both a nonlinear time-discretised and a linear time-harmonic FEA based on the $\boldsymbol{A}$–V formulation were conducted. They found that the calculations of the loss obtained from both of the cases were quite close in the clamping plate and the clamping fingers when just the fundamental of the excitation current was considered. However, when the 3rd harmonic was added, the calculations of the loss in the clamping fingers were still close in both of the cases, but there was a big difference between the calculations in the clamping plate.

Then Yao et al. (2006) analysed the distribution of the eddy currents in the finger plate and the clamping plate of a 1056-MVA turbogenerator by using the reduced magnetic vector potential and Biot-Savart's law. Moreover, in another paper written by Yao et al. (2008), the eddy currents in the clamping plate of a 1000-MW turbogenerator were analysed with the $\boldsymbol{A}$–V formulation. The authors found that the eddy currents were mainly distributed around the inner surface of the clamping plate. The corresponding eddy-current loss was also calculated under different operating conditions, such as no-load and full-load. In reference (Liang et al., 2008), by using the $\boldsymbol{A}$–V formulation, the authors briefly analysed the distribution of the eddy currents in the pressing plate of a 150-MW turbogenerator under no-load and under full-load, respectively.

In the above studies, the laminated stator core was modelled as a solid core with electrical and magnetic anisotropy — in other words, the laminations were not really modelled by reason of the extremely small thickness of both themselves and their insulation layers. However, Yamazaki et al. (2008) completed a calculation of the eddy currents in the stator core ends of a 250-MVA turbogenerator by using the FEM based on the $\boldsymbol{A}$–V formulation, and the laminations were really modelled in the finite element mesh used in their calculation.

2.3 Stator End-Winding Inductance

The leakage flux in the end region of radial flux electric machines includes mainly the leakage coming from the stator parts, e.g. the stator end winding, and the leakage coming from the rotor parts, e.g. the rotor end cage, but the most important leakage component is the stator end-winding leakage, which is usually represented by stator end-winding inductance.

Ban et al. (2005) completed an analytical calculation of the stator end-winding inductance of a 247-MVA turbogenerator by using a method based on Neumann's integral. They took full account of the 3-D structure of the end connections of the stator coils, especially the involute portion. The effect of the stator core was considered with the image method. By comparing their calculations with the measurements, they found that the calculations were close to the measurements when the relative permeability of the stator core was supposed to be zero — in other words, the stator core exhibited a highly impermeable effect. Another similar analytical calculation was performed by Schramm and Gerling (2005). The stator end-winding inductance of a switched reluctance machine was calculated with an analytical method quite similar to the one reported in reference (Ban et al., 2005). Additionally, Hsieh et al. (2007) carried out another analytical calculation. In their calculation, the end connections of the stator coils were considered to be semicircular. The magnetic induction was calculated from the magnetic vector potential, and then the end-winding inductance was determined from the flux linkage inside the end connections. The authors found their method fast and accurate in comparison with other analytical methods, but they did not discuss how effective the method would be when the real geometric shape of the end connections was considered.

Apart from the above analytical computations, most computations are based on numerical methods. In reference (Taieb Brahimi et al., 1993), the calculation of the stator end-winding inductance was based on the idea that the inductance of the whole stator winding varied as a linear function of the stator core length. In their calculation, the end region and the stator core ends of each machine were analysed from a 3-D model, but the middle portion of the core was analysed from a 2-D model. The end-winding inductance was determined by linear extrapolation; in other words, in terms of the relationship between the inductance of the whole stator winding and the core length, the end-winding inductance was extrapolated when the core length reached zero. Another numerical calculation was performed by Chiver et al. (2008). An idea, similar to the one reported in reference (Taieb Brahimi et al., 1993), was adopted in the calculation. Unlike Taieb Brahimi et al., the authors calculated the inductance of a portion of the stator winding lying in the active region of each machine by using a 2-D model, and then they estimated the end-winding inductance of each machine by subtracting the above inductance from the inductance of the whole stator winding, which was calculated from a 3-D model.

Cox et al. (2008) also studied the topic of the end-winding inductance, but they focused on the concentrated modular winding used in PM machines. The same procedure as in reference (Chiver et al., 2008) was used, i.e. a combination of a 2-D and a 3-D numerical model. In terms of the numerical calculations, they developed an analytical equation in order to conveniently estimate the end-winding inductance of the concentrated modular winding of a certain type of machines. Liang and Chen (2001) completed a calculation of the end-winding inductance of a 600-MW turbogenerator by using a quasi-3-D method. The authors investigated the accuracy of the calculations under different conditions, i.e. with and without the modelling

of the eddy currents in the end region, and with different rotor core lengths but a fixed stator core length.

In reference (de Weerdt and Belmans, 1995), not only the end-winding inductance but also other types of leakage inductance of an induction machine were thoroughly discussed. The authors first used a current-driven 2-D axisymmetric model and found that the end-ring inductance was heavily dependent upon the boundary conditions of the model. Next, in their current-driven 3-D model, the end-winding inductance, the end-ring inductance, and the mutual inductance between the end ring and the end winding were analysed, and they all depended on the slip. For instance, there was an increase in the mutual inductance when the slip increased, but a drop in both the end-ring inductance and the end-winding inductance appeared. Furthermore, in another paper written by de Weerdt et al. (1997), the authors analysed the importance of different end-region parameters of an induction machine, such as the end-winding inductance and the end-ring inductance, under different operating conditions, i.e. under no-load, full-load, and locked-rotor operation.

Different types of leakage inductance of large-sized electric machines were also calculated by Arshad et al. (2005), such as the end-winding inductance and the slot leakage inductance. The authors mainly analysed the accuracy of the calculations of the leakage inductance on the basis of different numerical models, such as 2-D models and 3-D models with and without radial cooling ducts.

2.4 End-Winding Forces and Vibrations

In radial flux electric machines running normally or abnormally, the time-varying end-winding forces cause mechanical vibrations of the end winding and its bracing system. The stresses and the strains in the end winding as well as in its bracing system are also partly related to the end-winding forces. The above aspects are closely correlated, so they are often considered together in the relevant literature.

Scott et al. (1981) calculated the steady-state end-winding forces of turbogenerators. In their analysis, the end-region magnetic field was supposed to vary sinusoidally in the circumferential direction and was solved with the FDM. The effect of the power factor on the end-winding forces was also analysed. In addition, as a continuation of reference (Scott et al., 1981), reference (Salon et al., 1983) was focused on the transient end-winding forces. In that paper, the spatial distribution of the forces under different kinds of malfunctions was shown, e.g. a 3-phase short circuit from full-load, and it was found that the transient forces tended to spread the end connections out.

Khan et al. (1989) also studied the transient end-winding forces in turbogenerators. A 1000-MW turbogenerator was analysed, with the current in the field winding as

well as in the damper winding considered. The spatial distribution of the forces under a 3-phase short circuit from full-load was also shown, which is similar to the distribution reported in reference (Salon et al., 1983). Then, in a paper written by Wen et al. (1996), the transient end-winding forces in a 35-MW turbogenerator under other kinds of malfunctions, such as a line-to-line short circuit and a line-to-neutral short circuit, were investigated.

Kim et al. (2005) completed an analysis of the transient end-winding forces during the starting of a high-voltage induction motor. The authors compared the end-winding forces among different phase belts and then analysed the reliability of the insulation layer of the end connections in terms of the stresses there. Liu and Hjärne (2007) performed a numerical calculation of the end-winding forces in a 635-MVA turbogenerator under full-load and a 3-phase short circuit from no-load. The authors calculated the force vectors by introducing a local coordinate system, which was defined in different positions of the end connections. They found that the forces always tended to spread the end connections out, whether under full-load or under the short circuit. It was also revealed that the forces on the two layers of the end winding could be attraction or repulsion. Additionally, in an analysis performed by Stancheva and Iatcheva (2009), in addition to the end-winding forces, the forces exerted on the stator core ends of a 200-MW turbogenerator were calculated with the Maxwell stress tensors.

Among the studies dealing with the end-winding vibrations, Patel and Butler (1983) analysed the relationship between the power factor and the end-winding vibrations of large-sized synchronous generators. The vibration patterns measured in various positions of the stator end winding were shown. By analysing the effect of the power factor and the core vibrations on the end-winding vibrations, the authors found that the end-winding vibrations were significantly strengthened under capacitive power factors and that there was a strong coupling between the core vibrations and the end-winding vibrations. Lambrecht and Berger (1983) systematically studied the mechanical properties of the integrated end-winding bracing system of turbogenerators. The authors measured the end-winding vibrations under three conditions: unexcited motor-driven operation to determine the relationship between the end-winding vibrations and the rotor speed; no-load operation to determine the end-winding vibrations caused by the core vibrations, and short-circuit operation to determine the end-winding vibrations caused by the forces. On the basis of the measurements, the effect of the vibration components with different frequencies on the amplitude of vibration was investigated.

Additionally, Léger and Szylowicz (1997) published a paper on the modelling of the end-winding vibrations of two turbogenerators. In their paper, a proportional damping model (Rayleigh damping model) was used in the viscous damping matrix of the governing equation. They also outlined the effect of the deterioration of the bracing system, e.g. the looseness of the wedges in the nose portion. In a paper written by Zhang et al. (1998), the authors summarised the consequences of the

end-winding vibrations in turbogenerators. The method used for the measurement and the method used for reinforcing the end-winding vibrations were explained.

Drubel et al. (2000) analysed the end-winding deformation in different turbogenerators under full-load and a 3-phase short circuit. The authors considered different kinds of design of the end-winding bracing system and found that the temperature-dependent stiffness of the tapes had a major effect on both the natural frequencies and the degree of deformation. Furthermore, they revealed that the resonant frequencies of the end winding were related to the change in the temperature.

Another important aspect is to monitor the long-term end-winding vibrations in turbogenerators. In reference (Demcko et al., 2007), a complete procedure for monitoring the end-winding vibrations based on fibre-optic accelerometers was explained in detail. In recent years, artificial intelligence algorithms, e.g. neural networks, have often been employed in order for the analysis of the variables to be monitored. For instance, van Wyk and Hoffman (2002) used a feedforward network in order to identify the long-term trend of the vibrations from the short-term end-winding fluctuations, and an auto-associative network in order to reduce the number of input variables.

Among the studies dealing with the stresses and the strains in the end winding, Ohtaguro et al. (1980) completed an analysis of the mechanical properties of the stator end winding in a 900-kW induction motor during its starting. At first, the authors found that the strains in the insulation layer of the end connections were dependent upon the number of spacers and their positions. Next, they ran a bending test for the coils with different kinds of insulation layers and concluded that the nonlinear relationship between the deflection and the bending moment must be taken into consideration in the course of calculating the deflections and the strains. Additionally, in reference (Merkhouf et al., 2003), the von Mises stresses in the end-winding bracing system of a 110-MVA synchronous generator under the transient operation were calculated. The authors found that the stresses calculated at two possible resonant frequencies were much lower than the corresponding yield stress.

In a paper written by Nagano et al. (2008a), the authors analysed the forces on the end winding with connection rings and those on the end winding without connection rings, and found that the effect of the current in the connection rings on the forces was negligible. They also performed a modal analysis of the above two end windings, and concluded that the difference between the two calculated modal models was quite small. Furthermore, in their another study reported in reference (Nagano et al., 2008b), the method of analysing the end-winding vibrations is similar to the one reported in reference (Lambrecht and Berger, 1983) — in other words, the rotation of the rotor and the core vibrations were both taken into account. The authors also analysed the stresses in the insulation layer of the end connections, which were caused by the end-winding forces and the thermal expansion. It was found that the largest stress appeared in the vicinity of the knuckle portion.

2.5 Summary

Many studies relating to the end region of large-sized radial flux electric machines, especially turbogenerators, have been carried out so far, and most of them are focused on the aforementioned aspects: the magnetic field, the eddy currents, the end-winding inductance, and the forces and vibrations.

First, an analysis of the end-region magnetic field is basic to an analysis of the other aspects. Analytical and numerical methods both have been adopted in the analysis, but the FEM is the most common method currently. With the FEM, the magnetic field has been solved with the two-potential method, or the $\boldsymbol{A}$–V formulation, or the $\boldsymbol{T}$–ϕ formulation. In fact, the $\boldsymbol{A}$–V formulation is suitable for the 2-D FEA of the cross-sectional model of radial flux electric machines in which the magnetic field and the winding circuit supplied from a voltage source are coupled and solved together at the same time. However, the $\boldsymbol{T}$–ϕ formulation is quite effective when most of the analysed domain is free of current (Nakata et al., 1988), e.g. the end region of electric machines, but more attention should be paid to the cancellation problem, which occurs in the iron part with high permeability (Nakata et al., 1990). Nowadays, most commercial FEA software packages use the $\boldsymbol{A}$–V formulation.

Second, the eddy currents related to the end-region magnetic field have been studied by numerical methods, especially the FEM, on the basis of either the $\boldsymbol{A}$–V or the $\boldsymbol{T}$–ϕ formulation. Most of the analyses are focused on the eddy currents in the metal parts of the end region, e.g. the clamping plate, as well as in the laminations of the core ends of turbogenerators. Actually, with a suitable coordinate system, the $\boldsymbol{T}$–ϕ formulation is effective in modelling the 2-D eddy currents inside the plane of the laminations because $\boldsymbol{T}$ can have only one axial component, T_z, which is perpendicular to the plane of the laminations. However, the eddy currents inside the end shield and the end frame of large-sized electric machines have not been analysed yet.

Third, in the analytical calculation of the stator end-winding inductance, a combination of Neumann's integral and the image method is normally used in order for the inclusion of the effect of the stator core. In fact, most of the calculations are based on the analysis of the magnetic energy, which is usually calculated with the FEM. The idea of those numerical calculations is that the inductance of the total stator winding, including the end-winding inductance, is a linear function of the stator core length, so the end-winding inductance can be derived from linear extrapolation.

Fourth, the end-winding forces in turbogenerators have been analysed as Lorentz forces, mostly with numerical methods, especially under the transient operation, e.g. under a 3-phase short circuit. In the course of the analysis of the corresponding vibrations, the amplitude of vibration, the resonant frequencies, and the stresses

in the end connections are the main issues. The effect of the core vibrations and the power factor on the end-winding vibrations has also been discussed. However, only the end-winding vibrations in turbogenerators are covered, and the vibrations appearing in large-sized induction machines have not been reported in detail.

Although all the aforementioned aspects of the end region have been studied, some issues have still not been covered, such as the eddy currents inside the end shield and the end frame as well as their effect on the end-region magnetic field, etc. In particular, the electromagnetic and the mechanical phenomena in the end region of large-sized induction machines have not been studied so much, and therefore analysing these phenomena in large-sized induction machines is the main focus in this piece of research.

3 Basic Introduction to Finite Element Analysis

This chapter outlines the FEA of the end-region magnetic field and the end-winding mechanical vibrations performed in this piece of research. The basic theory of electromagnetic fields and mechanical vibrations is briefly given as well. Detailed implementation of the FEA is not stated owing to the use of a commercial software package.

3.1 Finite Element Analysis of End-Region Magnetic Field

The 3-D, time-varying electromagnetic field in rotating electric machines can be solved through Maxwell's equations. The differential form of the relevant Maxwell's equations is

$$\nabla \times \boldsymbol{E} = -\frac{\partial \boldsymbol{B}}{\partial t} \tag{3.1}$$

$$\nabla \times \boldsymbol{H} = \boldsymbol{J} + \frac{\partial \boldsymbol{D}}{\partial t} \tag{3.2}$$

where $\boldsymbol{E}$ denotes the electric field strength, $\boldsymbol{B}$ the magnetic induction, t the time, $\boldsymbol{H}$ the magnetic field strength, $\boldsymbol{J}$ the conduction current density, and $\boldsymbol{D}$ the electric flux density. The displacement current density $\partial \boldsymbol{D}/\partial t$ in (3.2) can be omitted because the following relation holds under quasi-static conditions:

$$\frac{\partial \boldsymbol{D}}{\partial t} \ll \boldsymbol{J}. \tag{3.3}$$

In addition, related constitutive relations are

$$\boldsymbol{H} = \boldsymbol{\nu} \cdot \boldsymbol{B} \tag{3.4}$$

$$\boldsymbol{J} = \boldsymbol{\sigma} \cdot \boldsymbol{E} \tag{3.5}$$

where $\boldsymbol{\nu}$ and $\boldsymbol{\sigma}$ denote the tensor reluctivity and the tensor conductivity, respectively.

With the introduction of the magnetic vector potential $\boldsymbol{A}$ defined by $\boldsymbol{B}$, i.e.

$$\boldsymbol{B} = \nabla \times \boldsymbol{A}, \tag{3.6}$$

and the introduction of the electric scalar potential V, (3.1) is transformed into

$$\boldsymbol{E} = -\frac{\partial \boldsymbol{A}}{\partial t} - \nabla V. \tag{3.7}$$

By the above (3.3)–(3.7), (3.2) is transformed into

$$\nabla \times [\boldsymbol{\nu} \cdot (\nabla \times \boldsymbol{A})] + \boldsymbol{\sigma} \cdot \frac{\partial \boldsymbol{A}}{\partial t} + \boldsymbol{\sigma} \cdot \nabla V = 0. \tag{3.8}$$

In eddy-current problems, (3.8) is valid in the region in which eddy currents are considered. Moreover, when there are some known source currents in the region in which there are no eddy currents, the source current density $\boldsymbol{J}_{\mathrm{s}}$ can be added in (3.8), i.e.

$$\nabla\times[\boldsymbol{\nu}\cdot(\nabla\times\boldsymbol{A})]+\boldsymbol{\sigma}\cdot\frac{\partial\boldsymbol{A}}{\partial t}+\boldsymbol{\sigma}\cdot\nabla V-\boldsymbol{J}_{\mathrm{s}}=0. \tag{3.9}$$

In (3.9), there are either source currents or eddy currents in any current-carrying region, but not both. Actually, it is the governing equation of the $\boldsymbol{A}$–V formulation commonly used in the 3-D FEA of the electromagnetic field in electric machines as the current in the winding is normally considered a known source current. In addition, in the region in which eddy currents are considered, the continuity of current should be satisfied:

$$\nabla\cdot\left(\boldsymbol{\sigma}\cdot\frac{\partial\boldsymbol{A}}{\partial t}+\boldsymbol{\sigma}\cdot\nabla V\right)=0. \tag{3.10}$$

When the field quantities are supposed to vary sinusoidally in the time domain, the time dependence of (3.9) and (3.10) can be eliminated through a use of complex vectors and phasors. Under the circumstances, (3.9) and (3.10) become

$$\nabla\times[\boldsymbol{\nu}\cdot(\nabla\times\underline{\boldsymbol{A}})]+\mathrm{j}\omega\boldsymbol{\sigma}\cdot\underline{\boldsymbol{A}}+\boldsymbol{\sigma}\cdot\nabla\underline{V}-\underline{\boldsymbol{J}}_{\mathrm{s}}=0 \tag{3.11}$$

$$\nabla\cdot(\mathrm{j}\omega\boldsymbol{\sigma}\cdot\underline{\boldsymbol{A}}+\boldsymbol{\sigma}\cdot\nabla\underline{V})=0 \tag{3.12}$$

where a line under a symbol denotes the complex vector or the phasor of the field quantity symbolised by the symbol, ω the angular frequency, and j the imaginary unit.

In fact, the above forms a theoretical part of the $\boldsymbol{A}$–V formulation. The $\boldsymbol{A}$–V formulation has been widely adopted in many software packages relating to the FEA of electromagnetic fields, e.g. COMSOL Multiphysics$^{\mathrm{TM}}$.

From a mathematical point of view, solving the electromagnetic field in electric machines is equivalent to seeking a solution to a complicated boundary value problem (BVP) described by its differential equation, e.g. (3.9). Numerical methods have been widely used for solving such complicated BVPs because of their feasibility and accuracy. In this piece of research, the analysis of the 3-D end-region magnetic field in large-sized squirrel-cage induction machines was based on the FEM, and the corresponding FEA was completed with COMSOL Multiphysics$^{\mathrm{TM}}$, on the basis of the $\boldsymbol{A}$–V formulation.

When the magnetic field in radial flux electric machines is solved from $\boldsymbol{A}$ by 2-D cross-sectional models in which the geometric structure and the material properties are independent of the axial position, $\boldsymbol{A}$ has just one axial component, A_z. The potential component A_z is a scalar quantity, so nodal elements, in which scalar shape functions are associated with the nodes of finite elements, are used for seeking

a piecewise planar function to approximate the distribution of A_z. With nodal elements, the values of A_z at the free nodes of finite elements are solved, and A_z is continuous across the interface between any two neighbouring finite elements.

However, the end-region magnetic field must be considered in 3-D space, so $\boldsymbol{A}$ has all its r-, φ-, and z-component, A_r, A_φ, and A_z, where r, φ, and z denote the radial, the circumferential, and the axial coordinate, respectively. Obviously, what needs to be solved is a vector quantity. Although it is still possible to use nodal elements to solve $\boldsymbol{A}$, e.g. in reference (Keskinen, 1992), edge elements, in which vector shape functions are associated with the edges of finite elements, are widely used in the FEA of 3-D magnetic fields instead of nodal elements. With edge elements, the values of the tangential component of $\boldsymbol{A}$ along the free edges of finite elements are solved. They can also ensure the continuity of the tangential field component across the interface between any two neighbouring finite elements and can leave the normal field component discontinuous (Kameari, 1990; Webb, 1993; Mur, 1994). Therefore, it is possible to solve a 3-D magnetic field directly from its field quantities, e.g. $\boldsymbol{H}$. As pointed out by Jin (1993), edge elements can overcome some shortcomings of nodal elements: the occurrence of spurious solutions which is attributed to a lack of enforcement of the divergence condition; the inconvenience of applying boundary conditions to material interfaces as well as conducting surfaces, and the difficulty in treating conducting and dielectric edges and corners due to the field singularities associated with these structures. A detailed explanation of edge elements lies beyond the scope of this compendium, but it can be found in relevant books, e.g. in references (Jin, 1993) and (Volakis et al., 1998).

In COMSOL Multiphysics$^{\text{TM}}$, edge elements and nodal elements are used for discretising the distribution of the magnetic vector potential $\boldsymbol{A}$ and the electric scalar potential V, respectively. In addition, the discretisation with the FEM is based on the weak formulation of the weighted residual formulation of the differential equation, and the weighted residual formulation is completed with Galerkin's method. In all the FEAs of the end-region magnetic field performed in this piece of research, because of the limited computational resources, first-order tetrahedral and first-order prismatic edge elements were used for discretising the 3-D distribution of $\boldsymbol{A}$ in the end region and in the active region of the induction machines, respectively, but no gauge condition was applied to $\boldsymbol{A}$.

3.2 Finite Element Analysis of End-Winding Vibrations

There is no difference between the mechanical vibrations in electric machines and the vibrations of other dynamic systems. In general, there are two approaches to studying the vibrations of a dynamic system: a force approach and an energy approach. The force approach is based on Newton's second law of motion and the energy approach is based on the energy conservation principle. The energy approach

is suitable for approximate computer methods, e.g. the FEM (Doyle, 2004).

The energy approach is related to the principle of virtual work. On the basis of this approach, the governing equation of the motion of a dynamic system can be derived from Lagrange's equation of motion, which uses generalised coordinates that are independent of each other and equal in number to the DOFs of the system. For a linear dynamic system with translational motion described by its N generalised coordinates, the Lagrange's equation of motion given in reference (Doyle, 2004) is

$$\frac{\mathrm{d}}{\mathrm{d}t}\left(\frac{\partial E_{\mathrm{k}}}{\partial \dot{q}_j}\right) - \frac{\partial E_{\mathrm{k}}}{\partial q_j} + \frac{\partial}{\partial q_j}\left(E_{\mathrm{s}} + E_{\mathrm{p}}\right) - Q_j = 0, \quad j = 1, \cdots, N, \tag{3.13}$$

where a dot over a symbol denotes the first derivative of the field quantity symbolised by the symbol with respect to time, j the index, q_j generalised coordinate j, E_{k} the kinetic energy of the system, E_{s} the strain energy of the system, E_{p} the potential energy of the system, and Q_j the generalised force associated with q_j. Among the above physical quantities, E_{p} is related to the conservative forces, but Q_j is related to the nonconservative forces.

As fully described in reference (Doyle, 2004), when the motion of the dynamic system is small, with a Taylor series expansion about its equilibrium position "0", the kinetic energy can be obtained as

$$E_{\mathrm{k}} \approx \frac{1}{2}\sum_{j=1}^{N}\sum_{k=1}^{N} M_{jk}\dot{q}_j\dot{q}_k \tag{3.14}$$

where k denotes the index, q_k generalised coordinate k, and

$$M_{jk} = \left.\frac{\partial^2 E_{\mathrm{k}}}{\partial \dot{q}_j \partial \dot{q}_k}\right|_0 . \tag{3.15}$$

Similarly, the strain energy can be obtained as

$$E_{\mathrm{s}} \approx \frac{1}{2}\sum_{j=1}^{N}\sum_{k=1}^{N} K_{jk}q_j q_k \tag{3.16}$$

where

$$K_{jk} = \left.\frac{\partial^2 E_{\mathrm{s}}}{\partial q_j \partial q_k}\right|_0 , \tag{3.17}$$

and the potential energy can be obtained as

$$E_{\mathrm{p}} = -\sum_{j=1}^{N} F_j q_j \tag{3.18}$$

where

$$F_j = -\left.\frac{\partial E_{\mathrm{p}}}{\partial q_j}\right|_0 \tag{3.19}$$

where F_j denotes the external force associated with generalised coordinate q_j.

When the nonconservative forces of the system are considered as viscous forces, Q_j can be derived from a potential function called Rayleigh's dissipation function, D, as

$$Q_j = -\frac{\partial D}{\partial \dot{q}_j} \tag{3.20}$$

where

$$D \approx \frac{1}{2} \sum_{j=1}^{N} \sum_{k=1}^{N} C_{jk} \dot{q}_j \dot{q}_k \tag{3.21}$$

where

$$C_{jk} = \left. \frac{\partial^2 D}{\partial \dot{q}_j \partial \dot{q}_k} \right|_0 . \tag{3.22}$$

With (3.14), (3.16), (3.18), (3.20), and (3.21), the Lagrange's equation of motion can be organised in a form of matrix as

$$\boldsymbol{M}\ddot{\boldsymbol{q}} + \boldsymbol{C}\dot{\boldsymbol{q}} + \boldsymbol{K}\boldsymbol{q} = \boldsymbol{F} \tag{3.23}$$

where $\boldsymbol{M}$ denotes the mass matrix whose entries are shown in (3.15), $\boldsymbol{C}$ the viscous damping matrix whose entries are shown in (3.22), $\boldsymbol{K}$ the stiffness matrix whose entries are shown in (3.17), $\boldsymbol{q}$ a column vector of the generalised coordinates, $\boldsymbol{F}$ a column vector of the external forces whose entries are shown in (3.19), and two dots over a symbol denote the second derivative of the field quantity symbolised by the symbol with respect to time.

As a matter of fact, the above forms a part of the basic theory of the mechanical vibrations of dynamic systems. Lagrange's equation of motion is based on generalised coordinates, but (3.23) can be applied to displacement analyses as well providing that the coordinates are measured from a fixed reference system, as pointed out by Vierck (1979). In addition, (3.23) is a governing equation used in many software packages relating to the FEA of mechanical vibrations, e.g. COMSOL Multiphysics$^{\text{TM}}$, which was used in this piece of research in order for the analysis of the end-winding vibrations.

In general, the end-winding vibrations in electric machines should be analysed in 3-D space because of the 3-D structure of the end winding. In other words, the displacement caused by the vibrations has all its r-, φ-, and z-component. In COMSOL Multiphysics$^{\text{TM}}$, nodal elements are used for discretising the distribution of the displacement. In all the FEAs of the end-winding vibrations performed in this piece of research, second-order tetrahedral nodal elements were used for the discretisation.

4 Electromagnetic Analysis of End Region

This chapter outlines the electromagnetic FEA of the end region of two large-sized 3-phase squirrel-cage induction machines. The FEA covers three aspects: an analysis of the end-region magnetic field, a calculation of the stator end-winding inductance, and an analysis of the eddy currents inside the end shield and the end frame. A detailed account of the above three aspects is not provided in this chapter, but it can be found in Publications I–III.

4.1 End-Region Magnetic Field

The end-region magnetic field in a 3-phase, 4-pole, 2.24-MW squirrel-cage induction machine was analysed. The main parameters of the machine are listed in Appendix A as Machine I. The rotor was removed so that the motor could be tested in the laboratory. The machine has a two-layer diamond winding consisting of insulated form-wound multi-turn coils. A diamond winding was selected in the FEA because its model was easier to built with commercial software packages than other kinds of windings, e.g. random windings commonly used in low-voltage electric machines (Sadarangani, 2000). In fact, diamond windings are commonly used in radial flux electric machines with a power range of 1 MW and above, and a voltage range of 1 kV – 30 kV (Sadarangani, 2000). Their detailed description can be found in many books, such as references (Liwschitz-Garik and Whipple, 1946), (Holmberg, 1998), and (Sadarangani, 2000).

The model of the end connections was built by the measurements of the 3-D coordinates in different positions of a certain end connection, and each end connection in the model was made up of 22 connective segments. The multi-turn coils were modelled as single-turn solid coils. The laminated core was modelled as a homogeneous solid core with magnetic and electrical anisotropy. As in references (Bastos and Quichaud, 1985) and (Silva et al., 1995b), from the corresponding equivalent reluctance, its axial reluctivity was determined from

$$\nu_{\mathrm{Fe},z} = \nu_{\mathrm{lam}} k_{\mathrm{Fe}} + \nu_0 \left(1 - k_{\mathrm{Fe}}\right) \tag{4.1}$$

where $\nu_{\mathrm{Fe},z}$ denotes the axial reluctivity of the core, ν_{lam} and ν_0 the reluctivity of the laminations and that of vacuum, respectively, and k_{Fe} the stacking factor of the core. The axial conductivity of the solid core was considered to be zero because of the insulation layers on the surface of the laminations. In fact, the laminated core was stacked with non-oriented electrical steel sheets instead of grain-oriented ones, but the non-oriented ones still had higher permeability in their rolling direction. In the process of manufacturing the core, the laminations were rotated with respect to each other so that the magnetic properties of the core could be as isotropic as

possible in the plane of the laminations. Therefore, in this piece of research, the magnetic and the electrical properties of the solid core were considered isotropic in all directions perpendicular to the axial direction. In addition, because of the periodicity and the symmetry of the magnetic field, only one pole at one end of the machine was modelled, but the model did not include the rotor. Figure 4.1 shows the finite element mesh of the end region and that of a certain end connection.

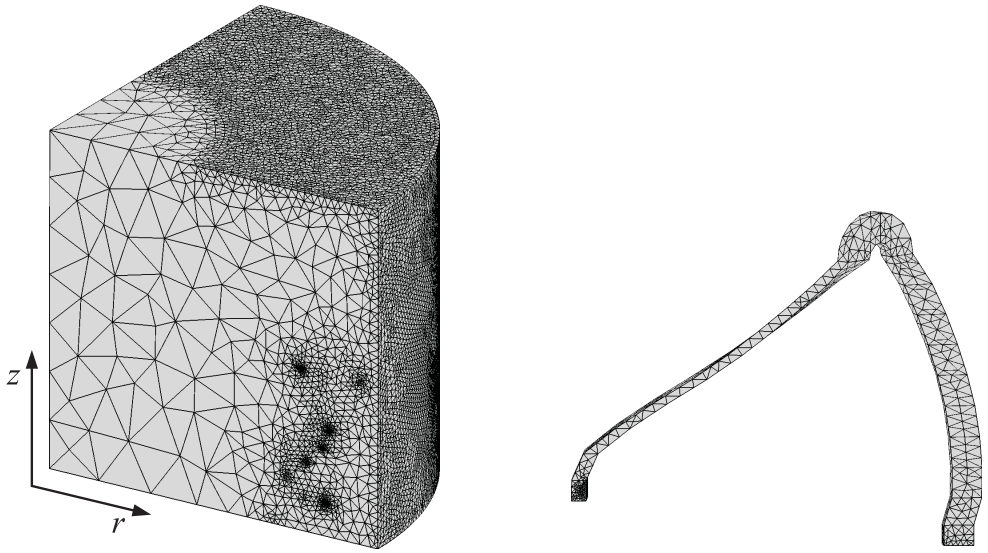

(a) (b)

Figure 4.1: The finite element mesh of the model of a 3-phase, 4-pole, 2.24-MW squirrel-cage induction machine. (a) The finite element mesh of the end region. (b) The finite element mesh of a certain end connection.

The current in the end winding of the model was supplied from a current source. The nonlinearity of the ferromagnetic materials was not taken into consideration because a nonlinear calculation had to be carried out by a time-discretised FEA requiring extremely long computation time. Therefore, a time-harmonic FEA was performed. As the time dependence of the field quantities was eliminated in the time-harmonic FEA, the reluctivity used in the approximation should be independent of time. As pointed out by Arkkio (1987), an approximation of the sinusoidal time-variation was only reasonable when root-mean-square (rms) values were calculated under the steady state, so it was normally a good choice to define the reluctivity of the ferromagnetic materials as a function of the rms value of the magnetic induction. However, it was not possible to define the reluctivity as mentioned above in the commercial software package used. It was also difficult to give different values of the reluctivity in the ferromagnetic parts having different degrees of saturation, e.g. the laminations, in the commercial software package. Therefore, a 2-D time-discretised FEA based on a cross-sectional model of the same machine was completed in order for the examination of the average reluctivity over the plane of the laminations.

From the calculations, the unsaturated reluctivity was around $1.74 \times 10^{-4}\nu_0$, and there was an increase in the reluctivity as the magnetic field was strengthened. At the rated operating point, it was around $2.64 \times 10^{-4}\nu_0$. Because of the skin effect, the actual reluctivity of the core could be even larger. As a result, a common value of the reluctivity, $0.001\nu_0$, was used in the solid core. The use of this value definitely caused an error in the calculation of the magnetic field inside the core, but the end-region magnetic field was hardly affected in terms of the measurements. This value was used in the end shield and the end frame as well.

The governing equation of the FEA was based on (3.11), but the term $\boldsymbol{\sigma}\cdot\nabla\underline{V}$ was dropped because of the limited computational resources. As a matter of fact, in the eddy-current region, $\boldsymbol{\sigma}\cdot\nabla\underline{V}$ in (3.11) always reduced the flow of the eddy currents, and therefore, from the viewpoint of eddy currents, the omission of $\boldsymbol{\sigma}\cdot\nabla\underline{V}$ represented a worst case scenario. For instance, in Section 4.3, the calculations based on a simple model show that the eddy-current loss inside the end shield and the end frame becomes around 10% smaller when $\boldsymbol{\sigma}\cdot\nabla\underline{V}$ is included. The term $\mathrm{j}\omega\boldsymbol{\sigma}\cdot\underline{\boldsymbol{A}}$ in (3.11) is the dominant part of the eddy currents. As a result, the actual governing equation of the FEA is

$$\nabla\times[\boldsymbol{\nu}\cdot(\nabla\times\underline{\boldsymbol{A}})]+\mathrm{j}\omega\boldsymbol{\sigma}\cdot\underline{\boldsymbol{A}}-\underline{\boldsymbol{J}}_{\mathrm{s}}=0. \tag{4.2}$$

The boundary conditions of the model were analysed, in particular, the boundary conditions dealing with the end shield and the end frame made from construction steel. The skin depth of those parts was around 1 mm at 50 Hz when its reluctivity was $0.001\nu_0$. According to Bastos and Sadowski (2003), it was necessary to discretise the eddy-current region into small finite elements in order for good precision. However, if the finite element mesh there had been generated accurately, a large number of finite elements would have been generated and the computer would not have been able to solve such a problem. Therefore, those parts had to be replaced by suitable boundary conditions.

In the FEA, three kinds of boundary conditions were applied to the inner surface of those parts, as shown in Figure 4.2. The corresponding three cases are explained below.

- Case 1: A homogeneous Dirichlet boundary condition was applied as

$$\underline{\boldsymbol{A}}\times\boldsymbol{n}=0 \tag{4.3}$$

  where $\boldsymbol{n}$ denotes a normal unit vector. According to Morisue (1988), the boundary condition meant that the normal component of $\boldsymbol{B}$ vanished within the inner surface of those parts.

- Case 2: A homogeneous Neumann boundary condition was applied as

$$\nabla\times\underline{\boldsymbol{A}}\times\boldsymbol{n}=0. \tag{4.4}$$

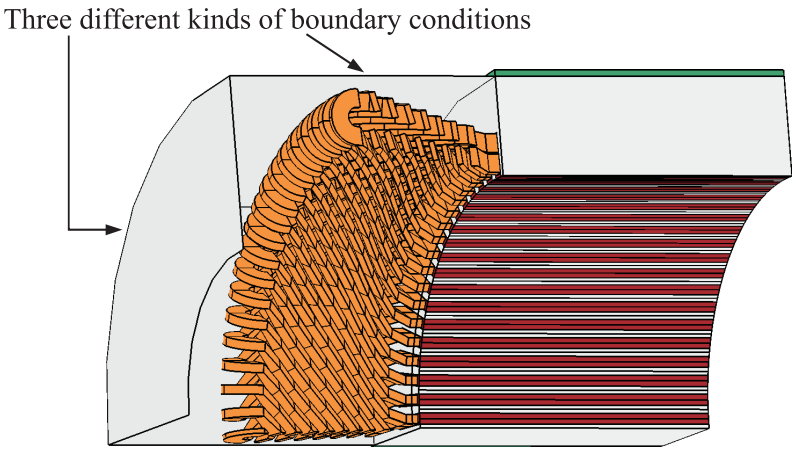

Figure 4.2: Three different kinds of boundary conditions applied to the inner surface of the end shield and the end frame. (Source: Publication I.)

It meant that the tangential component of $\boldsymbol{B}$ vanished within the inner surface of those parts.

- Case 3: In order that the eddy currents within the inner surface of those parts could be modelled, the SIBC was applied as

$$\boldsymbol{n} \times \underline{\boldsymbol{E}} = Z_{\mathrm{s}} \boldsymbol{n} \times (\boldsymbol{n} \times \underline{\boldsymbol{H}}) \tag{4.5}$$

where Z_{s} denotes the surface impedance.

In sum, in terms of the results obtained from the measurement performed in the following three cases: underload current (500 A), full-load current (832 A), and overload current (1000 A), the nonlinearity caused by the saturation is not distinct in the end region in all the three cases, by comparison with the nonlinearity in the active region. In the case of full-load current, the discrete Fourier transform (DFT) of the time-varying induced electromotive force (EMF) of the search coil in the end region indicates that a 5th and a 7th time harmonic arise in the end-region magnetic field, in addition to the fundamental, but they are quite weak. The results also show that the axial magnetic induction is the dominant component within the surface of the end shield but the radial magnetic induction is the dominant one within the surface of the end frame. In addition, the induced EMF of the search coils, the voltage of the stator phase winding, and the magnetic induction in the end region were measured respectively. In comparison with the measurements, the time-harmonic FEA based on all the above boundary conditions can obtain acceptable calculations of the end-region magnetic field, but the calculations based on the boundary conditions listed in cases 2 and 3 are more accurate. For instance, Table 4.1 lists a comparison between the induced EMFs from the FEA and the ones from

the measurement, where $\mathscr{E}_{\mathrm{end}}$ and $\mathscr{E}_{\mathrm{act}}$ denote the induced EMF of the search coils in the end region and in the active region, respectively, and a tilde over a symbol denotes the rms value of the field quantity symbolised by the symbol. It clearly shows that in cases 2 and 3, the results of the EMF of the search coil in the end region are very close to the measurements. A concrete and detailed analysis of the end-region magnetic field in the induction machine can be found in Publication I.

Table 4.1: Induced EMF of Search Coils.

Current (A)	Quantity	Finite Element Analysis			Measurement
		Case 1	Case 2	Case 3	
500	$\tilde{\mathscr{E}}_{\mathrm{end}}$ (V)	0.31	0.35	0.34	0.36
	$\tilde{\mathscr{E}}_{\mathrm{act}}$ (V)	3.23	3.24	3.24	3.58
832	$\tilde{\mathscr{E}}_{\mathrm{end}}$ (V)	0.52	0.58	0.57	0.61
	$\tilde{\mathscr{E}}_{\mathrm{act}}$ (V)	5.38	5.40	5.40	5.61
1000	$\tilde{\mathscr{E}}_{\mathrm{end}}$ (V)	0.63	0.70	0.69	0.73
	$\tilde{\mathscr{E}}_{\mathrm{act}}$ (V)	6.47	6.49	6.50	6.86

4.2 Stator End-Winding Inductance

The stator end-winding inductance of a 3-phase, 6-pole, 1.25-MW squirrel-cage induction machine was calculated. The main parameters of the machine are listed in Appendix A as Machine II. The machine has a two-layer diamond winding consisting of form-wound multi-turn coils.

The way in which the model of the stator end winding was built is similar to the one described in Section 4.1. The multi-turn coils were modelled as single-turn solid coils, and the laminated core was modelled as a homogeneous solid core with the same magnetic and electrical anisotropy as in Section 4.1. Only one pole at one end of the machine was modelled, but the rotor was not included. The current in the end winding of the model was supplied from a current source. A linear B–H curve was used in the ferromagnetic materials, as explained in Section 4.1 in detail. The governing equation of the FEA is (4.2), with the electric scalar potential V omitted, as explained in Section 4.1.

As yet, a unique definition of stator end-winding inductance has not been proposed, so different authors calculated it in different ways. For instance, de Weerdt and Belmans (1995) took account of the coupling between the stator and the rotor in their calculation, but most authors, such as Taieb Brahimi et al. (1993) and Arshad et al. (2005), did not consider the coupling. In this FEA, the above coupling between

the stator and the rotor was not covered. The stator end-winding inductance per phase was calculated because it could be used in corresponding 2-D coupled field–circuit FEAs as a parameter of the following circuit equation:

$$u^{\mathrm{str}} = R^{\mathrm{str}} i^{\mathrm{str}} + \frac{\mathrm{d}\psi^{\mathrm{str}}_{\mathrm{act}}}{\mathrm{d}t} + L^{\mathrm{str}}_{\sigma,\mathrm{end}} \frac{\mathrm{d}i^{\mathrm{str}}}{\mathrm{d}t} \tag{4.6}$$

where u^{str}, i^{str}, and R^{str} denote the voltage, the current, and the resistance of the stator phase winding, respectively, $L^{\mathrm{str}}_{\sigma,\mathrm{end}}$ the stator end-winding inductance per phase, and $\psi^{\mathrm{str}}_{\mathrm{act}}$ the flux linkage of the stator phase winding in the active region.

The calculation of $L^{\mathrm{str}}_{\sigma,\mathrm{end}}$ was based on the magnetic energy associated with the stator end winding — in other words, both the self-inductance of each end connection and the mutual inductance among different end connections were included. Under the time-harmonic analysis, the time average of the magnetic energy over one period was adopted. The following equation relating to the magnetic energy should hold:

$$\bar{W}_{\mathrm{m,tot}} = \bar{W}^{\mathrm{src}}_{\mathrm{m,act}} + \bar{W}^{\mathrm{src}}_{\mathrm{m,end}} = \bar{W}^{\mathrm{reg}}_{\mathrm{m,act}} + \bar{W}^{\mathrm{reg}}_{\mathrm{m,end}} \tag{4.7}$$

where a bar over a symbol denotes the time average of the field quantity symbolised by the symbol, $W_{\mathrm{m,tot}}$ the total magnetic energy, $W^{\mathrm{src}}_{\mathrm{m,act}}$ and $W^{\mathrm{src}}_{\mathrm{m,end}}$ the magnetic energy associated with the coil sides[5] and the magnetic energy associated with the end connections, respectively, and $W^{\mathrm{reg}}_{\mathrm{m,act}}$ and $W^{\mathrm{reg}}_{\mathrm{m,end}}$ the magnetic energy in the active region and the magnetic energy in the end region, respectively. In addition, the following relations should hold:

$$\bar{W}^{\mathrm{src}}_{\mathrm{m,act}} \propto l^{\mathrm{str}}_{\mathrm{Fe}} \tag{4.8}$$

$$\bar{W}^{\mathrm{src}}_{\mathrm{m,end}} = \text{constant} \tag{4.9}$$

where $l^{\mathrm{str}}_{\mathrm{Fe}}$ denotes the stator core length. Among these quantities, $\bar{W}^{\mathrm{src}}_{\mathrm{m,end}}$ was related to $L^{\mathrm{str}}_{\sigma,\mathrm{end}}$, but it was not possible to calculate $\bar{W}^{\mathrm{src}}_{\mathrm{m,end}}$ directly. As a result, the calculation of $\bar{W}^{\mathrm{src}}_{\mathrm{m,end}}$ had to depend on (4.7) — in other words, $\bar{W}_{\mathrm{m,tot}}$ and $\bar{W}^{\mathrm{src}}_{\mathrm{m,act}}$ had to be calculated first.

$\bar{W}_{\mathrm{m,tot}}$ was easy to calculate whereas the calculation of $\bar{W}^{\mathrm{src}}_{\mathrm{m,act}}$ should be considered carefully. $\bar{W}^{\mathrm{src}}_{\mathrm{m,act}}$ did not equal $\bar{W}^{\mathrm{reg}}_{\mathrm{m,act}}$ by reason of the effect of the stator end-winding leakage. Therefore, in the FEA, the active region of the model was evenly divided into 40 10-mm-thick slices perpendicular to the axial direction, as shown in Figure 4.3. Because the middle portion of the active region was supposed not to be affected by the end-winding leakage, the magnetic energy in each of those slices lying in the middle portion should be equal. In other words, the magnetic energy in those slices was only associated with the coil sides. Therefore, the time average of the magnetic energy calculated in any of those slices times 40 equalled $\bar{W}^{\mathrm{src}}_{\mathrm{m,act}}$. With the known

[5]In this compendium, the definition of the term "coil sides" is from reference (Gross, 2007), and the term "coil sides" means the portion of a coil that lies in the slots, as indicated in Figure 1.3.

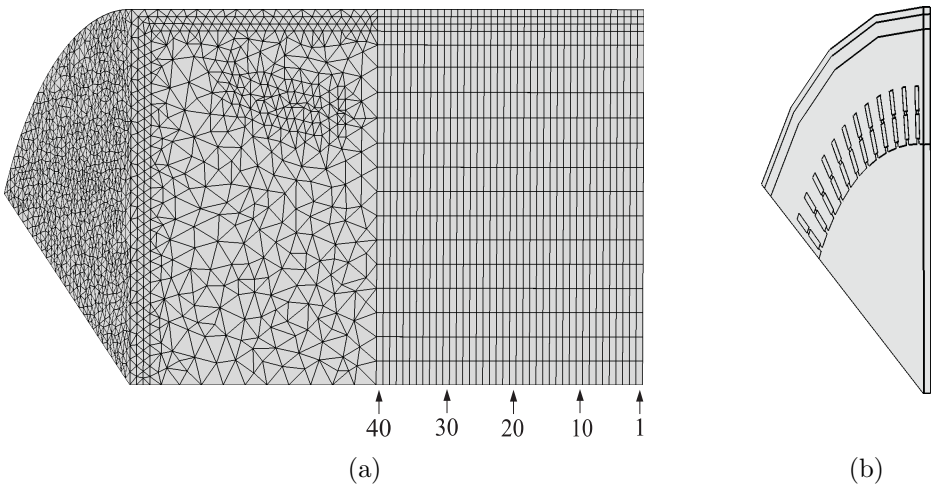

Figure 4.3: A general description of the slices used for calculating the magnetic energy. (a) The index of the slices in the active region of the model with the finite element mesh. (b) One of the slices in the active region. (Source: Publication II.)

$\bar{W}^{\mathrm{src}}_{\mathrm{m,act}}$ and $\bar{W}_{\mathrm{m,tot}}$, $\bar{W}^{\mathrm{src}}_{\mathrm{m,end}}$ was calculated from (4.7) and then $L^{\mathrm{str}}_{\sigma,\mathrm{end}}$ was calculated from

$$L^{\mathrm{str}}_{\sigma,\mathrm{end}} = 4p\,\frac{2\,\bar{W}^{\mathrm{src}}_{\mathrm{m,end}}}{m\left(\tilde{i}^{\mathrm{str}}\right)^2} \tag{4.10}$$

where p denotes the number of pole pairs, and m the number of phases. Additionally, the frequency dependence of the end-winding inductance and that of the magnetic energy mentioned above were analysed, and the excitation frequency was varied from 0.05 Hz to 5 kHz discretely.

In sum, the calculations of the magnetic energy in those 40 slices verify that only the slices close to the end surface of the core are affected by the end-winding leakage, as shown in Figure 4.4. In terms of the calculations at different frequencies, it is found that as the frequency goes up, $\bar{W}_{\mathrm{m,tot}}$ decreases but $\bar{W}^{\mathrm{src}}_{\mathrm{m,act}}$ remains constant. Therefore, there is a drop in $\bar{W}^{\mathrm{src}}_{\mathrm{m,end}}$, and correspondingly, $L^{\mathrm{str}}_{\sigma,\mathrm{end}}$ also decreases. The calculations prove that the following relations hold at any of the above frequencies:

$$\bar{W}^{\mathrm{src}}_{\mathrm{m,end}} \neq \bar{W}^{\mathrm{reg}}_{\mathrm{m,end}} \tag{4.11}$$

$$\bar{W}^{\mathrm{src}}_{\mathrm{m,act}} \neq \bar{W}^{\mathrm{reg}}_{\mathrm{m,act}}. \tag{4.12}$$

Moreover, because of the stator end-winding leakage, there is an increase in $\bar{W}^{\mathrm{reg}}_{\mathrm{m,act}}$ as the frequency increases, but both $\bar{W}^{\mathrm{src}}_{\mathrm{m,end}}$ and $\bar{W}^{\mathrm{reg}}_{\mathrm{m,end}}$ decrease. The drop in $\bar{W}^{\mathrm{reg}}_{\mathrm{m,end}}$ is more than the increase in $\bar{W}^{\mathrm{reg}}_{\mathrm{m,act}}$, which indicates that $\bar{W}_{\mathrm{m,tot}}$ decreases as the frequency goes up. It is speculated that the frequency dependence is related to the eddy currents in the end region as well as in the core ends. A concrete calculation of the end-winding inductance of the induction machine can be found in Publication II.

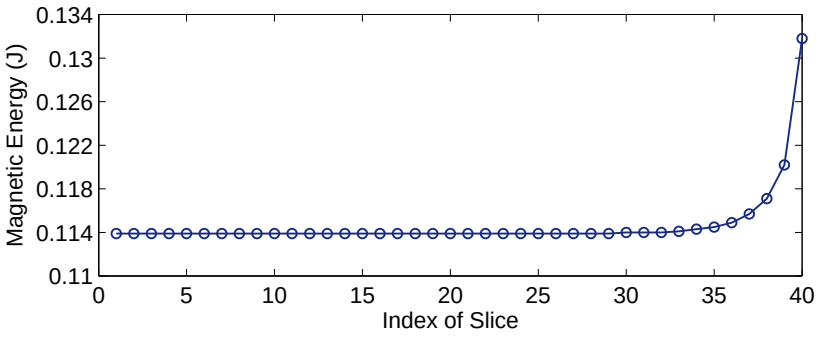

Figure 4.4: The time average of the magnetic energy at 50 Hz in each of the 40 slices in the active region. (Source: Publication II.)

4.3 Eddy Currents inside End Shield and End Frame

The electric machine used in this FEA is the same as the one in Section 4.1, and its main parameters can be found in Appendix A as Machine I. The eddy currents as well as the eddy-current loss inside the end shield and the end frame were analysed. The rotor was removed so that the machine could be tested in the laboratory.

The model of the stator end winding was built in terms of the measurements. However, in order that the eddy currents inside the end shield and the end frame could be analysed accurately with a dense finite element mesh, the model of the end winding was simplified — in other words, each end connection in the model was made up of 12 connective segments as shown in Figure 4.5. The multi-turn coils were modelled as single-turn solid coils, and the laminated core was modelled as a homogeneous solid core with the same magnetic and electrical anisotropy as in Section 4.1. Only one end of the machine was modelled, but the rotor was not included. The finite element mesh of the end region is similar to the one shown in Figure 4.1(a).

The current in the end winding of the model was supplied from a current source. On account of the extremely long computation time, a linear B–H curve was used in the ferromagnetic materials, as discussed in Section 4.1. The governing equation of the FEA is (4.2), with the electric scalar potential V dropped because of the limited computational resources, as explained in Section 4.1. Since in 3-D eddy-current problems, both the electric and the magnetic field must be described in the conductive region (Bíró and Preis, 1990), the neglect of V may lead to an inaccurate estimation of the eddy-current loss. Therefore, a simple model of the induction machine was built for analysing the effect of V on the eddy-current loss. The simple model is similar to the above model except that it included only one end connection; hence, it was capable of being solved by the computer under the $\boldsymbol{A}$–V formulation described by (3.11) and (3.12). The calculations showed that the eddy-current loss inside the end shield and the end frame was around 10% smaller

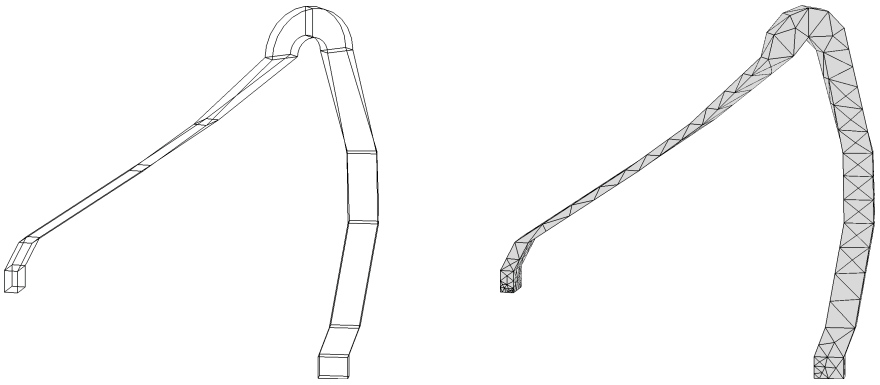

(a) (b)

Figure 4.5: A certain end connection of the model of a 3-phase, 4-pole, 2.24-MW squirrel-cage induction machine. (a) The 12 connective segments. (b) The finite element mesh.

when $\boldsymbol{\sigma}\cdot\nabla\underline{V}$ was included.

As explained in Section 4.1, the end shield and the end frame were not capable of being modelled because of the limited computational resources. They were more than 10 mm thick, but the skin depth there was just around 1 mm at 50 Hz when reluctivity $0.001\nu_0$ was used. Therefore, the eddy currents could be regarded as surface currents flowing within the inner surface of those parts. In this time-harmonic FEA, those surface currents were modelled with the SIBC listed in (4.5). In fact, the SIBC is based on the relation between the tangential component of the electric field and that of the magnetic field on the surface of the conductive region, and it allows only the surface of the region to be discretised (Gyselinck et al., 2009). A detailed explanation of the SIBC and its application can be found in relevant books and papers, such as references (Hoppe and Rahmat-Samii, 1995), (Jayasekera and Ciric, 2007), and (Alotto et al., 2007).

Since the eddy currents were considered as surface currents, the corresponding eddy-current loss was calculated from

$$\bar{P}_{\mathrm{Ft}} = \frac{1}{2}\iint_{\Gamma} \mathrm{Re}\left\{\underline{\boldsymbol{J}}_{\mathrm{sur}}\cdot\underline{\boldsymbol{E}}^{*}\right\}\mathrm{d}S \tag{4.13}$$

where P_{Ft} denotes the eddy-current loss, $\boldsymbol{J}_{\mathrm{sur}}$ the surface current density, Γ the surface of integration, S the surface area, and a star and "Re" beside a complex vector or a phasor denote the complex conjugate and the real part of the complex vector or the phasor, respectively.

In this analysis, how to validate the calculations of the eddy-current loss was a considerable problem. Though it was feasible to measure the total losses of the

induction machine, it was not possible to separate the loss inside the end shield and the end frame from the total losses. Consequently, an indirect method of measuring the temperature rise was adopted. In order for the measurement, a 1-mm-thick steel sheet was rolled up, and heat insulation filler was put around it. The steel sheet was then put into the end frame in such a way that it was tightly attached to the inner surface of the end frame. Owing to the small temperature differential between the winding and the steel sheet, the thermal radiation was negligible. The thermal conduction and the thermal convection were also omitted. As a result, the temperature rise in the steel sheet was attributed to the eddy-current loss there. Four thermocouples were fixed to the steel sheet in different axial positions for recording the change in temperature. The local dissipated power density in the steel sheet was estimated from

$$\overline{p}_{\mathrm{d}} = c_{\mathrm{stl}}\, \varrho_{\mathrm{stl}}\, \frac{\Delta \vartheta}{\Delta t} \tag{4.14}$$

where p_{d} denotes the dissipated power density, c_{stl} the specific heat capacity of steel, ϱ_{stl} the mass density of steel, $\Delta\vartheta$ the incremental temperature, and Δt the incremental time.

In the real machine, there are two main parameters related to the eddy-current loss inside the end shield and the end frame, and they are the minimum radial distance between the end frame and the end winding, r_{min}, and the minimum axial distance between the end shield and end winding, z_{min}, as indicated in Figure 4.6. From the viewpoint of electrical insulation, both of their minima can be around 7 mm. In order for the analysis of their effect on the eddy-current loss, some 3-D models were built. The above two parameters in every 3-D model were different, ranging from 7 mm to 40 mm. The eddy-current loss in each of the 3-D models was calculated with the same time-harmonic FEA as above. Additionally, the eddy-current loss was calculated from nonlinear time-discretised FEAs so that the effect of the magnetic nonlinearity in the end shield and the end frame could be analysed.

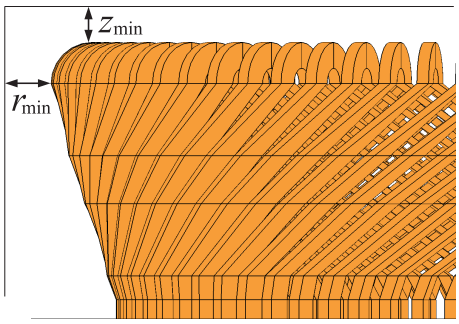

Figure 4.6: The minimum radial distance between the end frame and the end winding, r_{min}, and the minimum axial distance between the end shield and the end winding, z_{min}.

The nonlinear FEAs were carried out with simplified 2-D axisymmetric models for saving the computation time, and the above two parameters in every 2-D model were also different. A nonlinear single-valued B–H curve was applied to the end shield and the end frame of the 2-D models. The corresponding eddy-current loss was calculated from

$$\bar{P}_{\mathrm{Ft}}^{\varphi} = \frac{1}{T_1} \int_0^{T_1} \iint_{\Gamma} \sigma \left(\frac{\partial A_{\varphi}}{\partial t} \right)^2 \mathrm{d}S \, \mathrm{d}t \tag{4.15}$$

where $P_{\mathrm{Ft}}^{\varphi}$ denotes the eddy-current loss per unit circumferential length, and T_1 the period of the fundamental frequency.

In sum, the use of the SIBC to model the eddy currents inside the end shield and the end frame is feasible for large-sized induction machines. The measurement of the temperature rise is also a feasible solution to estimating the corresponding eddy-current loss. In terms of the 3-D time-harmonic FEAs, as shown in Figure 4.7, when

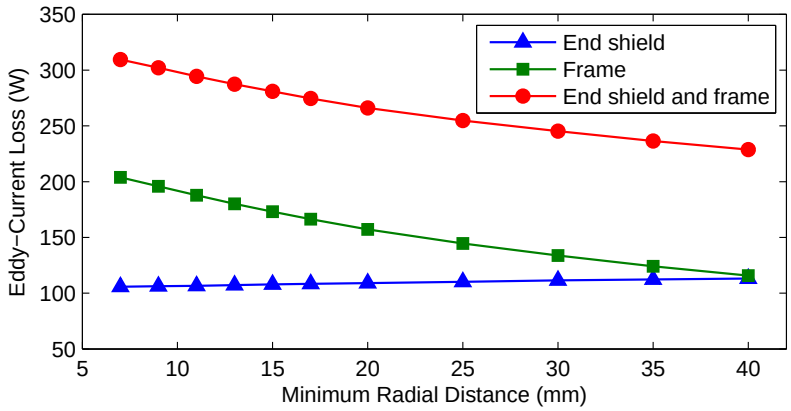

(a)

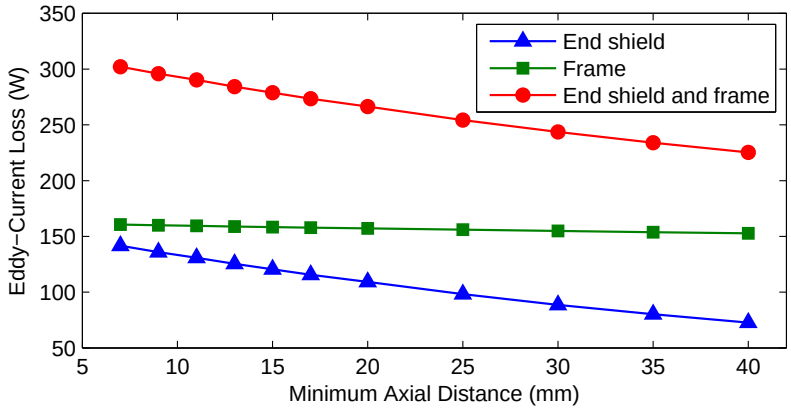

(b)

Figure 4.7: The variation in the eddy-current loss inside the end shield and the end frame of one end. (a) Only the minimum radial distance r_{min} is varied. (b) Only the minimum axial distance z_{min} is varied. (Source: Publication III.)

$r_{\min}$ and $z_{\min}$ are varied gradually from 7 mm to 40 mm, the eddy-current loss inside those parts also changes gradually. Relatively high loss density arises inside the end frame near the connection between the nose portion and the involute portion of the end connections, as shown in Figure 4.8, but the total loss is small in comparison with other types of loss, e.g. the copper loss of the stator phase winding. In the 2-D time-discretised FEAs, on the basis of the fact that the reluctivity was supposed to be $0.001\nu_0$ in the linear case, the eddy-current loss calculated in the nonlinear case under any combination of $r_{\min}$ and $z_{\min}$ is around 10% larger than the loss calculated in the corresponding linear case. A concrete and detailed analysis of the eddy currents and the corresponding eddy-current loss can be found in Publication III.

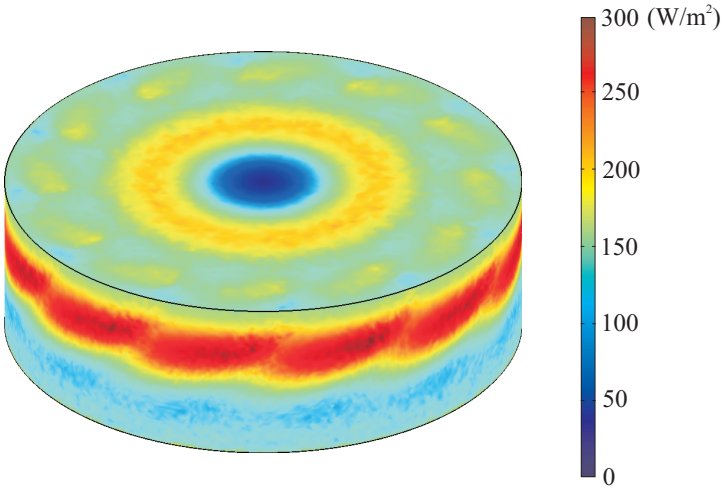

Figure 4.8: The distribution of the time average of the eddy-current loss density within the inner surface of the end shield and the end frame at $r_{\min} = 20$ mm and $z_{\min} = 20$ mm. (Source: Publication III.)

Only the eddy currents induced by the stator end-winding leakage were considered in the 3-D models of the squirrel-cage induction machine. The leakage flux coming from the rotor end cage was not covered since the rotor was not included in the FEAs. As a matter of fact, the position of the rotor end cage is far from the position of the end shield and the end frame in comparison with the position of the stator end winding, so their effect on the eddy-current loss is probably not so important as the effect of the stator end winding under the steady-state operation. However, with the rotor rotating, the resultant leakage field coming from the stator end winding as well as the rotor end cage may cause a new distribution of the 3-D end-region magnetic field; hence, there may be a change in the distribution of the eddy currents inside the end shield and the end frame as well.

5 Mechanical Analysis of End Region

This chapter outlines the mechanical FEA of the end region of two large-sized 3-phase squirrel-cage induction machines. The FEA covers two main aspects: an analysis of the end-winding magnetic forces and an analysis of the end-winding mechanical vibrations. A detailed account of the above two aspects is not provided in this chapter, but it can be found in Publications IV and V.

5.1 End-Winding Magnetic Forces

The magnetic forces exerted on the stator end winding of a 3-phase, 6-pole, 1.25-MW squirrel-cage induction machine under the steady-state full-load were analysed. The main parameters of the machine are listed in Appendix A as Machine II.

The way in which the 3-D model of the stator end winding was built is similar to the one described in Section 4.1. The multi-turn stator coils of the machine were replaced by single-turn solid coils in the model. A careful representation of the geometric shape of the end connections was of importance for the calculation of the end-winding forces, as pointed out by Lawrenson (1965), so each end connection was made up of 29 connective segments. In addition, in order that only one pole could be modelled, the number of rotor slots per pole should be an integer; hence, the number of rotor slots in the model was reduced from the original 86 to 84. According to Williamson and Ralph (1983), the rotor slot width should be changed accordingly so that the rotor tooth magnetomotive force drop could be kept the same. However, the rotor slot width was not changed since the calculation of the end-winding forces was the point of this analysis. Figure 5.1 shows part of the finite element mesh relating to the end region of the model.

The current in the end winding of the model was supplied from a current source. The magnetic nonlinearity of the ferromagnetic materials was not taken into account owing to the extremely long computation time, as explained in Section 4.1. As a result, a time-harmonic FEA was performed, in which the rotor of the model was supposed to be pseudostationary. The governing equation of the FEA was (4.2). The electric scalar potential V was not solved, as explained in Section 4.1. In the model, tensor conductivity $s\boldsymbol{\sigma}$ was used in the rotor, where s denotes the slip, so the frequency of the stator field was used in both the stator and the rotor. Furthermore, in order for a simplification of the numerical computation, the eddy currents inside the end shield and the end frame were omitted, so the boundary condition shown in (4.3) was applied to the inner surface of those parts.

The end-winding magnetic forces were classified as Lorentz forces. In the FEA of the 3-D model with 84 rotor slots, the steady-state forces on the end connections

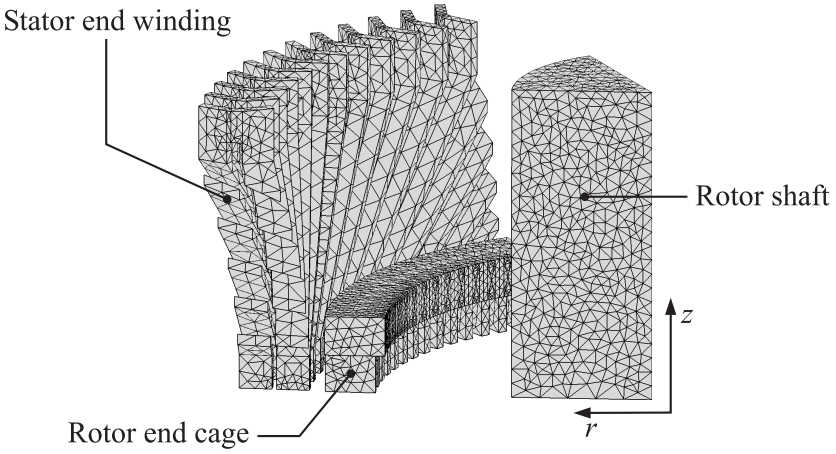

Figure 5.1: Part of the finite element mesh relating to the end region of the model of a 3-phase, 6-pole, 1.25-MW squirrel-cage induction machine.

of the three phase belts under a certain pole were somewhat different because the number of rotor slots per phase belt was not an integer. The time-varying end-winding forces on all the segments of the four end connections of a certain phase belt were calculated from

$$\boldsymbol{F}_{\mathrm{ew}} = \iiint_{\Omega} \boldsymbol{J} \times \boldsymbol{B} \, \mathrm{d}V \tag{5.1}$$

where $\boldsymbol{F}_{\mathrm{ew}}$ denotes the end-winding force, Ω the domain of integration, and V the volume. $\boldsymbol{B}$ was calculated from the FEA of the end-region magnetic field. The force components on a certain segment i were derived from (5.1). They are expressed as the following functions of time:

$$\begin{cases} F_{i,r} = \bar{F}_{i,r} + \hat{F}_{i,r,\sim} \cos\left(2\omega_{\mathrm{s}} t + \vartheta_{i,r0}\right) \\ F_{i,\varphi} = \bar{F}_{i,\varphi} + \hat{F}_{i,\varphi,\sim} \cos\left(2\omega_{\mathrm{s}} t + \vartheta_{i,\varphi 0}\right) \\ F_{i,z} = \bar{F}_{i,z} + \hat{F}_{i,z,\sim} \cos\left(2\omega_{\mathrm{s}} t + \vartheta_{i,z0}\right) \end{cases} , \qquad i = 1, \cdots, 29 \tag{5.2}$$

where a hat over a symbol denotes the amplitude of the field quantity symbolised by the symbol, i the index, $F_{i,r}$, $F_{i,\varphi}$, and $F_{i,z}$ denote the r-, the φ-, and the z-component of the force on segment i, ω_{s} the angular frequency of the stator field, $F_{i,r,\sim}$, $F_{i,\varphi,\sim}$, and $F_{i,z,\sim}$ the double-frequency force components, and $\vartheta_{i,r0}$, $\vartheta_{i,\varphi 0}$, and $\vartheta_{i,z0}$ the phase angles. Obviously, each force component consists of a constant and a double-frequency component.

Because the 29 connective segments of each end connection were not equal in volume, in order for a comparison of the force components on different segments of a certain end connection, the force density of a certain segment i was defined and calculated as

$$\boldsymbol{f}_i = \frac{\boldsymbol{F}_i}{V_i}, \qquad i = 1, \cdots, 29 \tag{5.3}$$

where $\boldsymbol{f}_i$ denotes the force density of segment i, $\boldsymbol{F}_i$ the force on segment i, and V_i the volume of segment i. The force density components of segment i are also expressed as the following functions of time:

$$\begin{cases} f_{i,r} = \dfrac{\bar{F}_{i,r}}{V_i} + \dfrac{\hat{F}_{i,r,\sim}}{V_i}\cos\left(2\omega_{\mathrm{s}}t + \vartheta_{i,r0}\right) \\ f_{i,\varphi} = \dfrac{\bar{F}_{i,}}{V_i} + \dfrac{\hat{F}_{i,\varphi,\sim}}{V_i}\cos\left(2\omega_{\mathrm{s}}t + \vartheta_{i,\varphi 0}\right) \\ f_{i,z} = \dfrac{\bar{F}_{i,z}}{V_i} + \dfrac{\hat{F}_{i,z,\sim}}{V_i}\cos\left(2\omega_{\mathrm{s}}t + \vartheta_{i,z0}\right) \end{cases} , \quad i = 1, \cdots, 29 \tag{5.4}$$

where $f_{i,r}$, $f_{i,\varphi}$, and $f_{i,z}$ denote the r-, the φ-, and the z-component of $\boldsymbol{f}_i$, respectively.

As a matter of fact, the most important six parameters in (5.4) are $\bar{F}_{i,r}/V_i$, $\hat{F}_{i,r,\sim}/V_i$, $\bar{F}_{i,\varphi}/V_i$, $\hat{F}_{i,\varphi,\sim}/V_i$, $\bar{F}_{i,z}/V_i$, and $\hat{F}_{i,z,\sim}/V_i$. These six parameters were calculated in all the segments of the four end connections of the phase belt. The calculations indicate that their values are basically larger in the knuckle portion of the end connections than in the nose portion and the involute portion. The largest radial force density appears in the knuckle portion lying in the inner layer of the end winding. The distribution of $\bar{F}_{i,r}/V_i$ and that of $\hat{F}_{i,r,\sim}/V_i$ among the four end connections are quite similar, in comparison with the distribution of the other four parameters relating to the circumferential and the axial force density. In addition, it is clearly found that $\bar{F}_{i,r}/V_i$, $\bar{F}_{i,\varphi}/V_i$, and $\bar{F}_{i,z}/V_i$ tend to spread all the end connections out in terms of their direction in different segments. A concrete and detailed analysis of the end-winding magnetic forces under the steady-state operation can mainly be found in Publication IV and partly in Publication V.

5.2 End-Winding Mechanical Vibrations

The end-winding mechanical vibrations caused by the steady-state end-winding forces in a 3-phase, 4-pole, 2.24-MW squirrel-cage induction machine were analysed. The main parameters of the machine can be found in Appendix A as Machine I. The rotor was removed because it was not possible to test the induction machine under full-load in the laboratory. The end connections of the multi-turn stator coils were braced by an end-winding bracing system. The bracing system included blocks, tapes, and rings, which were made from epoxy resin-impregnated glass fibre. The blocks were fixed between two neighbouring end connections for reducing their relative motion mainly in the φ-direction. The tapes were capable of fastening two end connections in the r-direction for restricting their relative motion mainly in the r- and the φ-direction. The rings surrounded all the end connections for restricting their motion mainly in the r-direction. Furthermore, the stator, including the end winding and its bracing system, had a global VPI process so that the end winding could possess good mechanical strength and good resistance to moisture and chem-

icals (Sadarangani, 2000; Pyrhönen et al., 2008). From a mechanical point of view, the end winding and its bracing system constituted a single entity.

In general, the function of the end-winding bracing system of large-sized radial flux electric machines is to make the end connections withstand large forces during starting and short circuits and to reduce end-winding vibrations (Sadarangani, 2000). It comprises non-conducting parts because of the electric field in the end region (Klempner and Kerszenbaum, 2004). The bracing system is very stiff in the r-direction for minimising the vibration level. However, it is allowed to move axially to accommodate the axial thermal expansion of the stator winding (Klempner and Kerszenbaum, 2004), because the forces resulting from the thermal expansion may reach a high level (Lambrecht and Berger, 1983). Though the bracing system can be made extremely stiff by a use of more bracing parts, such as blocks and rings, the cooling of the end region can be seriously affected.

The end-region magnetic field should be solved first before an analysis of the end-winding vibrations; hence, a complete model of the end region was required in order for the electromagnetic FEA. The complete model was called the electromagnetic model in this FEA. The insulated multi-turn coils were replaced by uninsulated single-turn solid coils in the model, so the insulation layers of the coils were not modelled. The laminated core was modelled as a homogeneous solid core with the same magnetic and electrical anisotropy as in Section 4.1. The end-winding bracing system was included in the electromagnetic model, but it was simplified on account of its complexity. The mechanical effect of the simplified bracing system was similar to that of the real one, but the effect of the enamel cured during the VPI process was not taken into consideration. Concerning the calculation of the vibrations, e.g. the calculation of a modal model, the mechanical model used was only a part of the electromagnetic model, which just included the end winding and its simplified bracing system.

The mechanical model was an LTI multi-DOF system, and Figure 5.2 shows part of the finite element mesh of the model. An undamped free-vibration FEA was completed in order for relevant modal data, which was based on the following governing equation:

$$\boldsymbol{M}\ddot{\boldsymbol{u}} + \boldsymbol{K}\boldsymbol{u} = 0 \tag{5.5}$$

where $\boldsymbol{u}$ denotes a column vector of the displacement. An impact hammer test, in which accelerance frequency response functions (FRFs) were measured, was completed in order for the experimental modal model. Only a column of entries of the accelerance FRF matrix was measured for the modal analysis according to He and Fu (2001) and Ewins (2000). The experimental modal model was compared with the calculated one derived from the FEA in order for possible model updating. In addition, in order that relevant correlated mode pairs (CMPs) could be identified, the modal assurance criterion (MAC) was calculated from the following expression

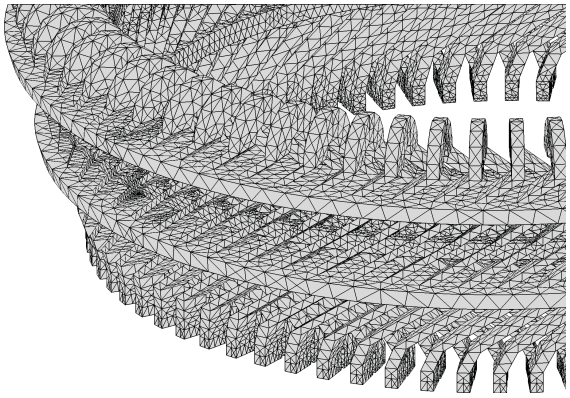

Figure 5.2: Part of the finite element mesh of the mechanical model of a 3-phase, 4-pole, 2.24-MW squirrel-cage induction machine.

given in reference (Allemang, 2003):

$$\mathrm{MAC}\left(\underline{\boldsymbol{\psi}}_{\mathrm{calc}}, \underline{\boldsymbol{\psi}}_{\mathrm{exp}}\right) = \frac{\left|\underline{\boldsymbol{\psi}}_{\mathrm{exp}}^{\mathrm{H}}\, \underline{\boldsymbol{\psi}}_{\mathrm{calc}}\right|^2}{\left(\underline{\boldsymbol{\psi}}_{\mathrm{exp}}^{\mathrm{H}}\, \underline{\boldsymbol{\psi}}_{\mathrm{exp}}\right)\left(\underline{\boldsymbol{\psi}}_{\mathrm{calc}}^{\mathrm{H}}\, \underline{\boldsymbol{\psi}}_{\mathrm{calc}}\right)} \tag{5.6}$$

where $\boldsymbol{\psi}_{\mathrm{exp}}$ and $\boldsymbol{\psi}_{\mathrm{calc}}$ denote a column vector of the experimental mode shape and a column vector of the calculated mode shape, respectively, and "H" near a symbol denotes the Hermitian transpose of the matrix symbolised by the symbol. Actually, the experimental mode shape vector was a vector of complex numbers whereas the calculated one was a vector of real numbers. After the comparison of the natural frequencies of the CMPs, according to Ewins (2000), the geometric structure of the model proved reasonable, but the material properties had to be updated because the simplifications made to the mechanical model changed its mechanical structure. As a result, the main elastic properties of the materials, i.e. the Young's modulus and the Poisson's ratio, were updated accordingly until the calculated modal model was close to the experimental one.

Next, a time-harmonic electromagnetic FEA, based on the governing equation (4.2), was performed for calculating the end-region magnetic field. The electric scalar potential V was not solved because of the limited computational resources, as explained in Section 4.1. In addition, a time-harmonic undamped forced-vibration FEA was carried out, which was based on the following governing equation:

$$\boldsymbol{M}\ddot{\boldsymbol{u}} + \boldsymbol{K}\boldsymbol{u} = \boldsymbol{F}_{\mathrm{exc}} \tag{5.7}$$

where $\boldsymbol{F}_{\mathrm{exc}}$ denotes a column vector of the excitation forces. The excitation forces were calculated from the previous electromagnetic FEA, and they were applied to the nodes of certain finite elements of the mechanical model by the software package since nodal elements were used in the mechanical FEA. Damping was omitted,

because the damping ratios derived from the impact hammer test were small and the excitation frequency was much lower than the natural frequency of the most excitable mode derived from the impact hammer test.

The constant force component and the double-frequency force component discussed in Section 5.1 were dealt with individually in the forced-vibration FEA because of the LTI characteristics of the mechanical model. Corresponding measurement of

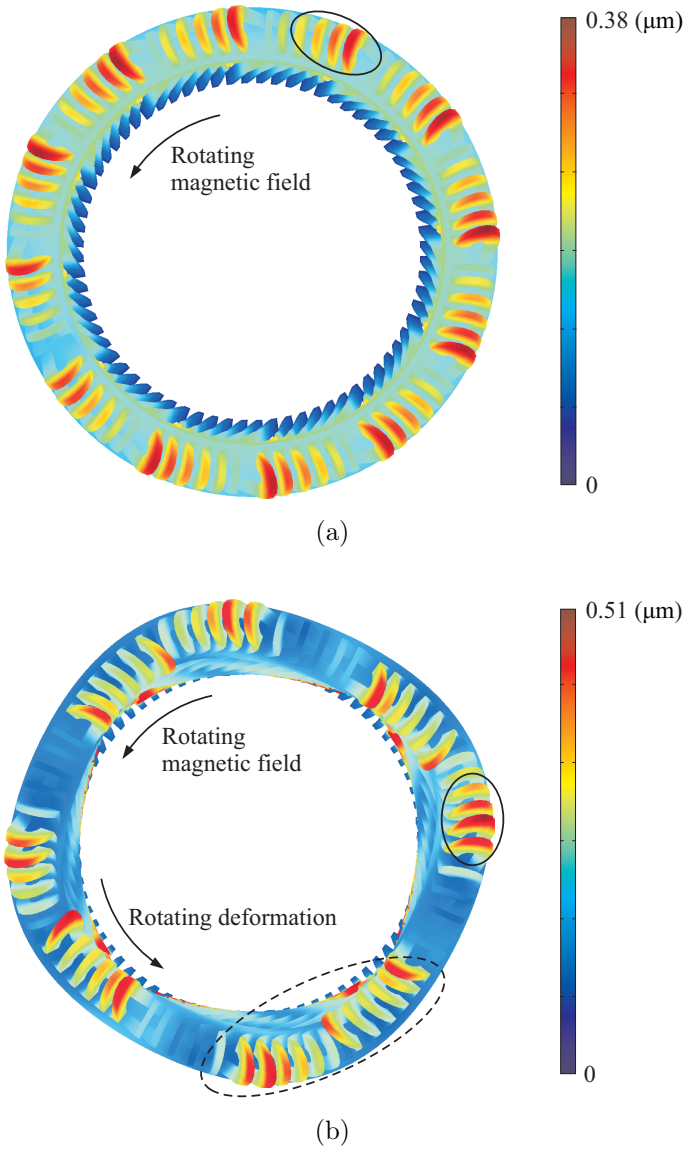

Figure 5.3: The deformation of the stator end winding and its bracing system. (a) The static deformation caused by the constant force component. (b) The dynamic deformation caused by the double-frequency force component. (Source: Publication V.)

the operating deflection shape (ODS) was also performed. Moreover, in order for an analysis of the metal fatigue of the copper conductors of the end connections, a calculation of the von Mises stresses and an analysis of the Goodman relationship were completed, respectively.

In sum, in terms of the results, both the constant force component and the double-frequency force component are larger in the knuckle portion and part of the involute portion of the end connections, but relatively strong deformation appears in the nose portion, as indicated by the ellipses in Figure 5.3. With the end-winding bracing system, the maximum amplitude of vibration is within 100 μm and the natural frequency of the most excitable mode, 315.6 Hz, is much higher than the excitation frequency, 100 Hz. The calculations based on the von Mises stresses and the Goodman relationship indicate that the metal fatigue of the copper conductors caused by the double-frequency force component is not an important issue. Furthermore, the frequency-spectrum analysis of the time-varying displacement, based on the DFT of the displacement components recorded during the ODS measurement, shows that in addition to the expected 100-Hz component, a strong 50-Hz component is present in the frequency spectrum. There are two reasons for the 50-Hz component: one is the interference coming from the electromagnetic sensitivity of the piezoelectric accelerometers, and the other is the current in the connection wire of the accelerometers. A concrete and detailed analysis of the end-winding mechanical vibrations under the steady-state operation can be found in Publication V.

6 Conclusions and Discussions

As the last chapter of this compendium, this chapter summarises the main results and discusses the scientific significance of this piece of research. Furthermore, some issues relating to the accuracy of the research methods are discussed.

6.1 Main Results of Research

The main results obtained from the electromagnetic and the mechanical FEA of the end region of the above two large-sized 3-phase squirrel-cage induction machines are divided into five aspects: the end-region magnetic field, the stator end-winding inductance, the eddy currents in the end region, the end-winding forces, and the end-winding vibrations.

First, a 3-D time-harmonic FEA of the end-region magnetic field is accurate enough. The magnetic nonlinearity caused by the saturation is not distinct in the end region. By comparison with the active region, the magnetic induction in the end region is quite weak, even near the knuckle portion of the end connections. The eddy currents inside the end shield and the end frame can be modelled with the SIBC, but they have only a slight effect on the end-region magnetic field. In fact, applying the SIBC or a homogeneous Neumann boundary condition to the inner surface of those parts can lead to an accurate analysis of the end-region magnetic field, but the use of a homogeneous Dirichlet boundary condition may cause some errors.

Second, the magnetic energy associated with the stator end winding can be separated from the magnetic energy associated with the whole stator winding by a 3-D FEA of the magnetic field in the end region and in the active region, as the end-winding leakage just affects the magnetic field in the core ends. The stator end-winding inductance can be calculated from the corresponding magnetic energy. Moreover, the magnetic energy in the end region does not equal the magnetic energy associated with the stator end winding, and the former is a little smaller than the latter.

Third, the eddy currents inside the end shield and the end frame can be regarded as surface currents, and it is feasible to apply the SIBC to the inner surface of those parts in order for modelling of the eddy currents with a 3-D time-harmonic FEA. Even if those parts are very close to the end winding, the corresponding eddy-current loss is still small. Furthermore, the eddy-current loss calculated in a 3-D time-harmonic FEA is somewhat smaller than that in the real situation because of the neglect of the saturation.

Fourth, the steady-state end-winding forces calculated in a 3-D time-harmonic FEA consist of a constant and a double-frequency component. The largest radial force

density appears in the knuckle portion of the end connections lying in the inner layer of the end winding. In a certain phase belt, the end-winding forces on each of the end connections are mostly different.

Fifth, in spite of the complexity of the end region, the end-winding vibrations can be analysed with a 3-D time-harmonic FEA based on an LTI mechanical model in which a simplified end-winding bracing system is used. However, because of the simplifications, modal testing is required in order for relevant modal data and possible model updating. With the end-winding bracing system, the maximum amplitude of vibration is quite small under the steady state. The natural frequency of the most excitable mode of the end winding and its bracing system is also raised to a high frequency avoiding resonances. Furthermore, the metal fatigue related to the cyclic loading cannot appear in the copper conductors of the end connections.

In sum, most of the important aspects relating to the end region of the two induction machines are covered in this piece of research. Although the modelling conditions used in the FEA are not exactly the same as the actual situation, the main results given above still provide a deep understanding of the end region, which is beneficial to the electromagnetic and mechanical design of the end region.

6.2 Scientific Significance of Research

This piece of research is mainly related to the design of large-sized radial flux electric machines. Although the end region is normally not so important in the analysis of electric machines as the active region, its fast and reliable 3-D FEA is more effective than its conventional analytical analysis and quasi-3-D FEA in the design and the optimisation of electric machines.

First, nowadays, a time-harmonic FEA is seldom used in the 2-D analysis of the active region of radial flux electric machines because a time-discretised FEA is no longer time-consuming on account of the development of computers. However, for the 3-D analysis of the end region, a time-discretised FEA is still too time-consuming to carry out. As a result, a 3-D time-harmonic FEA, together with a use of suitable boundary conditions, can be regarded as an efficient solution to the end-region magnetic field because it does not require much computation time but gives acceptable accuracy.

Second, by the method of calculating the stator end-winding inductance proposed in this piece of research, the magnetic energy associated with the stator end winding can be easily derived from a 3-D time-harmonic FEA based on a model with a fixed core length, instead of using many models with different core lengths for carrying out linear extrapolation. The method is not restricted to a time-harmonic FEA; conversely, it can be extended to a time-discretised FEA.

Third, the eddy-current loss inside the end shield and the end frame is small, even if the end winding is very close to those parts. However, the small loss does not mean that hot spots cannot appear because the distribution of the loss density is non-uniform. As relatively high loss density appears inside the end frame near the connection between the nose portion and the involute portion, the minimum radial distance between the end winding and the end frame is an important parameter. From the viewpoint of optimisation, the end frame can be shifted farther from the end winding in order for elimination of potential hot spots. By contrast, the minimum axial distance between the end winding and the end shield is not important since the loss density there is much smaller than that in the end frame.

Fourth, modelling the multi-turn stator coils and the complex end-winding bracing system in a mechanical FEA is normally accompanied by correction of the material properties of the model, in particular its elastic properties. In addition, under the steady-state operation, the knuckle portion experiences larger radial forces than the other portions, but relatively strong deformation and relatively large amplitude of vibration appear in the nose portion. However, the steady-state vibration levels are small, so the end-winding vibrations can hardly affect the end-region magnetic field. In other words, the interaction between the end-region magnetic field and the end-winding vibrations is negligible. If a stiffer end-winding bracing system is needed, more bracing parts can probably be fixed to the nose portion. The knuckle portion and the lower part of the involution portion seem not to require many bracing parts, and fewer bracing parts there are also beneficial to the cooling of the end region.

In sum, the above scientific significance covers both the FEA and the design of the end region. Though only squirrel-cage induction machines are covered in this piece of research, the above significance is also beneficial to other types of radial flux electric machines, such as wound rotor induction machines, wound field synchronous machines, and PM synchronous machines.

6.3 Accuracy of Research Methods

The FEA of the end region is the main part of this piece of research, and the corresponding measurement is a complement to the FEA. Neither the FEA nor the measurement is absolutely perfect. The following is a summary of the issues relating to the accuracy of the research methods.

1. Only the main parts in the end region were included in the 3-D models; for example, the bearings were not included. In order that boundary conditions could be applied conveniently in the model including the rotor, the rotor shaft was shortened, and it was completely inside the end region bounded by the end shield and the end frame. The insulated multi-turn stator coils

were replaced with uninsulated single-turn solid coils. The laminated core was modelled as a homogeneous solid core with magnetic and electrical anisotropy. The complex end-winding bracing system was also simplified.

2. As both the end region and at least part of the active region were required in the 3-D models, the number of DOFs could be greatly reduced with the use of prismatic edge elements in the active region, as shown in Figure 4.3(a). However, tetrahedral nodal and edge elements had to be used in the end region. When antiperiodic boundary conditions were applied, extremely narrow or irregular spaces were often generated somewhere in the end region. Tetrahedral elements in those spaces sometimes had an extremely low element quality, so the coefficient matrix of the system of equations was sometimes singular. Therefore, attention should be paid to the element quality.

3. The 3-D FEA of the end region did not take account of the following four main factors: the saturation of the ferromagnetic materials; the hysteresis of the ferromagnetic materials; the rotation of the rotor, and the mechanical nonlinearity of the structure. The first three are more important than the last one. The saturation can lower the peak magnetic induction in the saturated region and cause corresponding harmonics; the hysteresis can somewhat increase the loss in the ferromagnetic materials, and the rotation of the rotor can also cause higher harmonics, etc. Therefore, these three factors can somewhat affect the calculations of the end-region magnetic field and the eddy-current loss, etc. The reason why they were not considered in this piece of research results mainly from the limited computational resources and the extremely long computation time. The fourth factor is not important because the end-winding vibrations and the deformation were not large.

4. In the course of the modal testing of the 4-pole induction machine, the number of layers measured in the z-direction was three, and the number of spots measured in each layer in the φ-direction was eight. Actually, the three measured layers and the eight measured spots in each layer are not sufficient and are only able to show such mode shapes associated with lower natural frequencies roughly. More layers measured in the nose portion and more spots measured in each layer in the φ-direction will be advantageous to a complete description of the mode shapes and to finding modes with higher natural frequencies.

5. During the ODS measurement of the end-winding, the time-varying magnetic field in the machine interfered with the piezoelectric accelerometers. The interference can be eliminated by a use of fibre-optic accelerometers, as in references (Humer et al., 2008) and (Shally et al., 2008). On the other hand, in the course of the modal testing in which a piezoelectric accelerometer was also used, since no magnetic field was present in the machine, the above interference did not occur.

References

Allemang, R. J. (2003). The modal assurance criterion — Twenty years of use and abuse. *Sound Vib*, 37(8):14–21.

Alotto, P., De Cian, A., Molinari, G., and Rossi, M. (2007). Implementation of surface impedance boundary conditions in the cell method via the vector fitting technique. *COMPEL*, 26(3):859–872.

Arkkio, A. (1987). Analysis of induction motors based on the numerical solution of the magnetic field and circuit equations. *Acta Polytech Sc El*, (59).

Arshad, W. M., Lendenmann, H., Liu, Y., Lamell, J.-O., and Persson, H. (2005). Finding end winding inductances of MVA machines. In *Conf. Rec. 2005 IEEE Industry Applications Conf. 40th IAS Annual Meeting*, pages 2309–2314, Hong Kong, China.

Ban, D., Žarko, D., and Mandić, I. (2005). Turbogenerator end-winding leakage inductance calculation using a 3-D analytical approach based on the solution of Neumann integrals. *IEEE T Energy Conver*, 20(1):98–105.

Bastos, J. P. A. and Quichaud, G. (1985). 3D modelling of a non-linear anisotropic lamination. *IEEE T Magn*, MAG-21(6):2366–2369.

Bastos, J. P. A. and Sadowski, N. (2003). *Electromagnetic Modeling by Finite Element Methods*. Marcel Dekker, Inc., New York, NY, USA.

Bíró, O. and Preis, K. (1990). Finite element analysis of 3-D eddy currents. *IEEE T Magn*, 26(2):418–423.

Chiver, O., Micu, E., and Barz, C. (2008). Stator winding leakage inductances determination using finite elements method. In *Proc. 11th Int. Conf. Optimization of Electrical and Electronic Equipment*, pages 69–74, Brasov, Romania.

Chow, S. K., Lee, Y. T., and Owen, E. A. (1982). An integral-equation/singularity-method approach for 3-D electromagnetic field determination in the end region of a turbine-generator. *IEEE T Magn*, MAG-18(2):340–345.

Cox, T., Eastham, F., and Proverbs, J. (2008). End turn leakage reactance of concentrated modular winding stators. *IEEE T Magn*, 44(11):4057–4061.

de Weerdt, R. and Belmans, R. (1995). Squirrel cage induction motor end effects using 2D and 3D finite elements. In *Proc. 7th Int. Conf. Electrical Machines and Drives*, pages 62–66, Durham, UK.

de Weerdt, R., Tuinman, E., Hameyer, K., and Belmans, R. (1997). Finite element analysis of steady state behavior of squirrel cage induction motors compared with measurements. *IEEE T Magn*, 33(2):2093–2096.

Demcko, J., Velotta, J., and Tesla, A. (2007). New tools to monitor critical vibration of end-windings in turbo-generators. In *Proc. IEEE Int. Electric Machines and Drives Conf.*, pages 1020–1024, Antalya, Turkey.

Doyle, J. F. (2004). *Modern Experimental Stress Analysis: Completing the Solution of Partially Specified Problems*. John Wiley & Sons Ltd., Chichester, West Sussex, UK.

Drubel, O., Kulig, S., and Senske, K. (2000). End winding deformations in different turbo generators during 3-phase short circuit and full load operation. *Electr Eng*, 82(3-4):145–152.

Ewins, D. J. (2000). *Modal Testing: Theory, Practice and Application*. Research Studies Press Ltd., Baldock, Hertfordshire, England, UK, 2nd edition.

Frei-Spreiter, B. and Reichert, K. (1998). Calculation of end winding fields of turbogenerators by integral methods for modelling mechanical characteristics. *IEEE T Magn*, 34(5):3636–3639.

Fujita, M., Tokumasu, T., Yoda, H., Tsuda, H., Ito, K., and Nagano, S. (2000). Magnetic field analysis of stator core end region of large turbogenerators. *IEEE T Magn*, 36(4):1850–1853.

Gross, C. A. (2007). *Electric Machines*. CRC Press, Taylor & Francis Group, Boca Raton, FL, USA.

Gyselinck, J., Dular, P., Geuzaine, C., and Sabariego, R. V. (2009). Surface-impedance boundary conditions in time-domain finite-element calculations using the magnetic-vector-potential formulation. *IEEE T Magn*, 45(3):1280–1283.

He, J. and Fu, Z. (2001). *Modal Analysis*. Butterworth-Heinemann, Oxford, UK.

Ho, S. L. and Fu, W. N. (1998). Review and future application of finite element methods in induction motors. *Electr Pow Compo Sys*, 26(2):111–125.

Holmberg, M. T. (1998). *Three-Dimensional Finite Element Computation of Eddy Currents in Synchronous Machines*. PhD thesis, Chalmers University of Technology, Gothenberg, Sweden.

Hoppe, D. J. and Rahmat-Samii, Y. (1995). *Impedance Boundary Conditions in Electromagnetics*. Taylor & Francis, Washington, DC, USA.

Hsieh, M.-F., Hsu, Y.-C., Dorrell, D. G., and Hu, K.-H. (2007). Investigation on end winding inductance in motor stator windings. *IEEE T Magn*, 43(6):2513–2515.

Humer, M., Vogel, R., and Kulig, S. (2008). Monitoring of generator end winding vibrations. In *Proc. 2008 Int. Conf. Electrical Machines*, pages 1–5, Vilamoura, Portugal.

Jack, A. G. and Mecrow, B. C. (1986). Computation and validation against measurements of stator end-region fields in synchronous generators. *IEE Proc*, 133(1):26–32.

Jack, A. G. and Mecrow, B. C. (1987). A method to calculate turbogenerator end region fields and losses and validation using measured results. *IEEE T Energy Conver*, EC-2(1):100–107.

Jayasekera, K. A. S. N. and Ciric, I. R. (2007). Evaluation of surface impedance models for axisymmetric eddy-current fields. *IEEE T Magn*, 43(5):1991–1999.

Jin, J. (1993). *The Finite Element Method in Electromagnetics*. John Wiley & Sons, Inc., New York, NY, USA.

Kameari, A. (1990). Calculation of transient 3D eddy current using edge-elements. *IEEE T Magn*, 26(2):466–469.

Keskinen, E. (1992). Applicability of vector potentials in the finite element solution of three-dimensional eddy current problems. *Acta Polytech Sc El*, (71).

Khan, G. K. M., Buckley, G. W., Bennett, R. B., and Brooks, N. (1990). An integrated approach for the calculation of losses and temperatures in the end-region of large turbine generators. *IEEE T Energy Conver*, 5(1):183–194.

Khan, G. K. M., Buckley, G. W., and Brooks, N. (1989). Calculation of forces and stresses on generator end-windings — Part I: Forces. *IEEE T Energy Conver*, 4(4):661–670.

Kim, K.-C., Lee, H.-W., Chun, Y.-D., and Lee, J. (2005). Analysis of electromagnetic force distribution on end winding for motor reliance. *IEEE T Magn*, 41(10):4072–4074.

Klempner, G. and Kerszenbaum, I. (2004). *Operation and Maintenance of Large Turbo-Generators*. John Wiley & Sons, Inc., Hoboken, NJ, USA.

Lambrecht, D. and Berger, H. (1983). Integrated end-winding ring support for water-cooled stator winding: Design features, analysis, test results and experience. *IEEE T Power Ap Syst*, PAS-102(4):998–1006.

Lawrenson, P. J. (1965). Forces on turbogenerator end windings. *Proc IEE*, 112(6):1144–1158.

Lazarns, V. S., Kladas, A. G., Mamalis, A. G., and Tegopoulos, J. A. (2009). Analysis of end zone magnetic field in generators and shield optimization for force reduction on end windings. *IEEE T Magn*, 45(3):1470–1473.

Léger, A. C. and Szylowicz, N. (1997). Modelling the vibration behaviour of stator end windings. In *Proc. 8th Int. Conf. Electrical Machines and Drives*, pages 160–164, Cambridge, UK.

Li, J., Sun, Y., and Yang, G. (2005). Calculation and analysis of 3D magnetic field for end region of large turbogenerators. In *Proc. 8th Int. Conf. Electrical Machines and Systems*, pages 2079–2082, Nanjing, China.

Liang, Y. and Chen, W. (2001). Numerical calculation of stator end-leakage reactance of large turbogenerator. In *Proc. 5th Int. Conf. Electrical Machines and Systems*, pages 170–173, Shenyang, China.

Liang, Y., Huang, H., and Hu, G. (2008). Numerical calculation of end region electromagnetic field of large air-cooled turbogenerator. In *Proc. World Automation Congr.*, pages 1–5, Waikoloa, HI, USA.

Liang, Y., Lu, Y., Zhu, K., Ge, B., and Cai, W. (2003). Analysis and computation of 3D eddy current in turbogenerator rotor end region at asynchronous operation. In *Proc. IEEE Int. Electric Machines and Drives Conf.*, pages 415–418, Madison, WI, USA.

Liu, Y. and Hjärne, S. (2007). Analysis of forces on coil ends of formed stator windings. In *Proc. Int. Conf. Electrical Machines and Systems*, pages 1019–1024, Seoul, Korea.

Liwschitz-Garik, M. and Whipple, C. C. (1946). *Electric Machinery*. D. Van Nostrand Company, Inc., New York, NY, USA.

Mecrow, B. C., Jack, A. G., and Cross, C. S. (1989). Electromagnetic design of turbogenerator stator end regions. *IEE Proc*, 136(6):361–372.

Merkhouf, A., Boueri, B. F., and Karmaker, H. (2003). Generator end windings forces and natural frequency analysis. In *Proc. IEEE Int. Electric Machines and Drives Conf.*, pages 111–114, Madison, WI, USA.

Morisue, T. (1988). A new formulation of the magnetic vector potential method in 3-D multiply connected regions. *IEEE T Magn*, 24(1):110–113.

Mur, G. (1994). Edge elements, their advantages and their disadvantages. *IEEE T Magn*, 30(5):3552–3557.

Nagano, S., Tokumasu, T., Fujita, M., Ichimonji, M., Sekito, S., Hiramatsu, D., Nagakura, K., and Nitta, T. (2008a). Study on electromagnetic force in the end portion of large-capacity cylindrical synchronous generators: Improvement of reactance estimation and verification of electromagnetic force. *Electr Eng Jpn*, 163(4):67–77.

Nagano, S., Tokumasu, T., Fujita, M., Inoue, Y., Ichimonji, M., Katayama, H., Hiramatsu, D., and Nitta, T. (2008b). Study on vibration caused by electromagnetic force in the end portion of large-capacity cylindrical synchronous machines: Imporvement of electromagnetic force estimation and verification of degradation on winding insulation. *Electr Eng Jpn*, 163(4):78–89.

Nakata, T., Takahashi, N., Fujiwara, K., and Imai, T. (1990). Effects of permeability of magnetic materials on errors of the **T**–Ω method. *IEEE T Magn*, 26(2):698–701.

Nakata, T., Takahashi, N., Fujiwara, K., and Okada, Y. (1988). Improvements of the **T**–Ω method for 3-D eddy current analysis. *IEEE T Magn*, 24(1):94–97.

Novender, W.-R. and Müller, W. (1983). 3-dimensional nonlinear calculations of magnetic fields in turbogenerators. *IEEE T Magn*, MAG-19(6):2604–2607.

Ohtaguro, M., Yagiuchi, K., and Yamaguchi, H. (1980). Mechanical behavior of stator endwindings. *IEEE T Power Ap Syst*, PAS-99(3):1181–1185.

Patel, M. R. and Butler, J. M. (1983). End-winding vibrations in large synchronous generators. *IEEE T Power Ap Syst*, PAS-102(5):1371–1377.

Plantive, E., Salon, S., Chari, M. V. K., and Richard, N. (1996). Advances in the axiperiodic magnetostatic analysis of generator end regions. *IEEE T Magn*, 32(5):4278–4280.

Pyrhönen, J., Jokinen, T., and Hrabovcová, V. (2008). *Design of Rotating Electrical Machines*. John Wiley & Sons, Ltd., Chichester, West Sussex, UK.

Richard, S., Ducreux, J.-P., and Foggia, A. (1997). A three dimensional finite element analysis of the magnetic field in the end region of a synchronous generator. In *Rec. IEEE Int. Electric Machines and Drives Conf.*, pages WC2/4.1–WC2/4.3, Milwaukee, WI, USA.

Sadarangani, C. (2000). *Electrical Machines—Design and Analysis of Induction and Permanent Magnet Motors*. KTH Royal Institute of Technology, Stockholm, Sweden.

Salon, S. J. (1990). Finite element analysis of electric machinery. *IEEE Comput Appl Pow*, 3(2):29–32.

Salon, S. J., Scott, D. J., and Kusic, G. L. (1983). Electromagnetic forces on the end windings of large turbine generators. II. Transient conditions. *IEEE T Power Ap Syst*, PAS-102(1):14–19.

Schmidt, E., Traxler-Samek, G., and Schwery, A. (2005). Influence of higher harmonics in the end region magnetic field on eddy currents in the stator clamping system of hydro generators. In *Proc. IEEE Int. Electric Machines and Drives Conf.*, pages 1268–1274, San Antonio, TX, USA.

Schramm, A. and Gerling, D. (2005). Analytical calculation of the end winding leakage inductance based on the solution of Neumann integrals. In *Proc. IEEE Int. Symp. Industrial Electronics*, pages 851–855, Dubrovnik, Croatia.

Scott, D. J., Salon, S. J., and Kusik, G. L. (1981). Electromagnetic forces on the armature end windings of large turbine generators I — Steady state conditions. *IEEE T Power Ap Syst*, PAS-100(11):4597–4603.

Shally, D., Farrell, M., and Sullivan, K. (2008). Generator end winding vibration monitoring. In *Proc. 43rd Int. Universities Power Engineering Conf.*, pages 1–5, Padova, Italy.

Sikora, R., Gawrylczyk, K. M., Gramz, M., Gratkowski, S., and Ziółkowski, M. (1986). Magnetic field computation in the end-region of electric machines using various boundary conditions on iron surfaces. *IEEE T Magn*, MAG-22(3):204–207.

Sikora, R., Lipiński, W., Gawrylczyk, K. M., Gramz, M., Gratkowski, S., Pałka, R., and Ziółkowski, M. (1982). Analysis of the magnetic field in the end region of induction motor. *IEEE T Magn*, MAG-18(2):674–678.

Silva, V. C., Maréchal, Y., and Foggia, A. (1995a). Surface impedance method applied to the prediction of eddy currents in hydrogenerator stator end regions. *IEEE T Magn*, 31(3):2072–2075.

Silva, V. C., Meunier, G., and Foggia, A. (1995b). A 3-D finite-element computation of eddy currents and losses in laminated iron cores allowing for electric and magnetic anisotropy. *IEEE T Magn*, 31(3):2139–2141.

Silva, V. C., Meunier, G., and Foggia, A. (1996). A 3D finite-element computation of eddy currents and losses in the stator end laminations of large synchronous machines. *IEEE T Magn*, 32(3):1569–1572.

Stancheva, R. D. and Iatcheva, I. I. (2009). 3-D electromagnetic force distribution in the end region of turbogenerator. *IEEE T Magn*, 45(3):1000–1003.

Stone, G. C., Sasic, M., Dunn, D., and Culbert, I. (2009). Recent problems experienced with motor and generator windings. In *Rec. 56th Annual Petroleum and Chemical Industry Conf.*, pages 1–9, Anaheim, CA, USA.

Taieb Brahimi, A., Foggia, A., and Meunier, G. (1993). End winding reactance computation using a 3D finite element program. *IEEE T Magn*, 29(2):1411–1414.

Tang, R., Xu, G., Tian, L., Zhao, D., and Xu, Y. (1990). Calculation of end region magnetic field and circulating losses for turbo-generators using a coupled field and circuit equations method. *IEEE T Magn*, 26(2):497–500.

van Wyk, E. M. P. and Hoffman, A. J. (2002). Detecting long-term trends in turbogenerator stator end-winding vibrations through neural network modelling. *J Sound Vib*, 253(3):529–544.

Vierck, R. K. (1979). *Vibration Analysis*. Harper & Row, Publishers, Inc., New York, NY, USA, 2nd edition.

Volakis, J. L., Chatterjee, A., and Kempel, L. C. (1998). *Finite Element Method for Electromagnetics: Antennas, Microwave Circuits, and Scattering Applications*. IEEE Press, New York, NY, USA.

Webb, J. P. (1993). Edge elements and what they can do for you. *IEEE T Magn*, 29(2):1460–1465.

Weiss, J. and Stephens, C. M. (1981). Finite elements for three-dimensional magnetostatic fields and its application to turbine-generator end regions. *IEEE T Power Ap Syst*, PAS-100(4):1591–1596.

Wen, X., Yao, R., and Tegopoulos, J. A. (1994). Transient quasi-3D method in the transient electromagnetic field calculation of end region of turbo-generator. *IEEE T Magn*, 30(5):3709–3712.

Wen, X., Yao, R., and Tegopoulos, J. A. (1996). Calculation of forces on the stator end windings of turbogenerator by the transient quasi-3D method. *IEEE T Magn*, 32(3):1669–1672.

Williamson, S. and Ralph, J. W. (1982). Finite-element analysis for nonlinear magnetic field problems with complex current sources. *IEE Proc*, 129(6):391–395.

Williamson, S. and Ralph, J. W. (1983). Finite-element analysis of an induction motor fed from a constant-voltage source. *IEE Proc*, 130(1):18–24.

Yamazaki, K., Tada, S., Mogi, H., Mishima, Y., Kaido, C., Kanao, S., Takahashi, K., Ide, K., Hattori, K., and Nakahara, A. (2008). Eddy current analysis considering lamination for stator core ends of turbine generators. *IEEE T Magn*, 44(6):1502–1505.

Yao, Y., Xia, H., Ni, G., Liang, X., and Xian, Z. (2008). Analysis of magnetic-thermal coupled fields in the end region of large turbine-generators. In *Proc. World Automation Congr.*, pages 1–5, Waikoloa, HI, USA.

Yao, Y., Xia, H., Ni, G., Liang, X., Yang, S., and Ni, P. (2006). 3-D eddy current analysis in the end region of a turbogenerator by using reduced magnetic vector potential. *IEEE T Magn*, 42(4):1323–1326.

Zhang, J., Jiang, X., and You, Z. (1998). Vibration measurement of the generator stator end windings and precautions against insulation wearing. In *Proc. Int. Conf. Power System Technology*, pages 1021–1024, Beijing, China.

Appendix A Main Parameters of Electric Machines

Table A.1: Main Parameters of Induction Machines I and II.

	Machine I	Machine II
Parameter	Value	Value
Rated power (MW)	2.24	1.25
Rated voltage (V)	1000	690
Rated frequency (Hz)	50	50
Rated slip	0.37%	0.365%
Full length of stator core (mm)	1000	800
Full length of rotor core (mm)	1010	810
Outer diameter of stator core (mm)	980	980
Inner diameter of stator core (mm)	670	670
Outer diameter of rotor core (mm)	662	663
Number of phases	3	3
Number of pole pairs	2	3
Number of stator slots	72	72
Number of rotor slots	86	86
Number of layers of stator winding	2	2
Number of turns in series of stator coil	3	3
Number of parallel branches of stator winding	4	3
Coil span of stator coil (stator slot pitches)	16	10
Skewing of stator slots	0	0
Skewing of rotor slots	0	0
Connection of stator winding	Delta	Delta

ISBN 978-952-60-3285-6
ISBN 978-952-60-3286-3 (PDF)
ISSN 1795-2239
ISSN 1795-4584 (PDF)